Atomic-Level Insight into the Post Synthesis Bandgap Engineering of a Lewis Basic Polymer Using the Lewis Acid Tris(pentafluorophenyl)borane

Brett Yurash,[§,†] Dirk Leifert,[§,†] G. N. Manjunatha Reddy,[‡] David Xi Cao,[†] Simon Biberger,[†,⊥] Viktor V. Brus,[†] Martin Seifrid,[†] Peter J. Santiago,[†] Anna Köhler,[⊥] Bradley F. Chmelka,[‡] Guillermo C. Bazan,*[,†] Thuc-Quyen Nguyen*[,†]

[†]Center for Polymers and Organic Solids
Department of Chemistry and Biochemistry
University of California, Santa Barbara, Santa Barbara, CA 93106, United States of America

[‡]Department of Chemical Engineering
University of California, Santa Barbara, Santa Barbara, CA 93106, United States of America

[⊥]Department of Physics, Bayreuth Institute of Macromolecular Research (BIMF) and Bavarian Polymer Institute (BPI), University of Bayreuth, Universitätsstraße 30, 95447 Bayreuth, Germany

[§]Co-first author

*Corresponding author's E-mail: quyen@chem.ucsb.edu, bazan@chem.ucsb.edu

This paper is dedicated to Professor Jean-Luc Brédas on the occasion of his 65th birthday.

Abstract:

In this report, we investigate the binding properties of the Lewis acid tris(pentafluorophenyl)borane with a Lewis basic semiconducting polymer, PFPT, and the subsequent mechanism of bandgap reduction. Experiments and quantum chemical calculations confirm that the formation of a Lewis acid adduct is energetically favorable ($\Delta G° < -0.2$ eV), with preferential binding at the pyridyl nitrogen in the polymer backbone over other Lewis basic sites. Upon adduct formation, ultraviolet photoelectron spectroscopy indicates only a slight decrease in the HOMO energy, implying that a larger reduction in the LUMO energy is primarily responsible for the observed optical bandgap narrowing ($\Delta E_{opt} = 0.3$ eV). Herein, we also provide the first spatially resolved picture of how Lewis acid adducts form in heterogeneous, disordered polymer:tris(pentafluorophenyl)borane thin films via one- (1D) and two-dimensional (2D) solid-state nuclear magnetic resonance. Notably, solid-state 1D ^{11}B, $^{13}C\{^{1}H\}$ and $^{13}C\{^{19}F\}$ cross-polarization magic-angle spinning (CP-MAS) NMR and 2D $^{1}H\{^{19}F\}$ and $^{1}H\{^{1}H\}$ correlation NMR analyses establish that BCF molecules are intercalated between branched $C_{16}H_{33}$ sidechains with the boron atom facing towards the pyridyl nitrogen atoms of PFPT.

Motivation and Background:

A key advantage of organic semiconductors over inorganic counterparts is their ability to precisely tune the semiconductor's optical properties via synthetic modification.[1] Donor-acceptor (D-A) organic chromophores have become a particularly fruitful category of organic semiconductors with a wide variety of optical and electrical properties which has led to their incorporation in multiple technologies, such as organic photovoltaics (OPVs), organic field-effect transistors (OFETs), and organic light-emitting diodes

(OLEDs).[2–9] In these D-A molecular structures, there are alternating electron rich (D) and electron poor (A) moieties, resulting in excited states with significant intramolecular charge transfer (ICT) character. By tuning the relative strength of the donor and acceptor units, the optical bandgap (E_{opt}) can be tuned from the ultraviolet to the near-infrared. A post-synthesis strategy for tuning the optical properties of Lewis basic D-A type organic semiconductors via incorporation of Lewis acids was demonstrated by Welch et al. in 2009.[10] The resulting Lewis acid adducts showed red-shifted absorption, i.e. a reduction of the bandgap, to a degree consistent with the strength of the Lewis acid. Since then, this general strategy has been utilized by various research groups in order to adjust the optoelectronic properties of organic semiconductors with Lewis basic binding sites.[11–15] In particular, Lewis acids have been used to tune the emission of polymer light-emitting diodes (PLEDs)[16,17] and enhance the charge transport properties (via p-type doping) of vertical diodes,[18,19] solar cells,[20,21] OFETs,[22,23] and organic thermoelectric devices.[24]

$B(C_6F_5)_3$ has been the Lewis acid of choice due to its strong Lewis acidity, relative stability to air and to moisture, resistance to B-C bond cleavage, and high solubility in a variety of organic solvents.[25–27] While there has been considerable investigation into the changes in optical properties upon adduct formation in conjugated polymers, atomic-level interactions that account for the binding mechanism, with concomitant electronic and thermodynamic descriptions, have remained poorly understood. X-ray diffraction studies of Lewis acid adduct single crystals have shed insight on the nature of bonding interactions between the Lewis acid and Lewis basic sites of small molecule organic chromophores, e.g. pyrroles and indoles, providing details such as boron-nitrogen bonding distances.[10,28–30] However, for polymers exhibiting multiple different Lewis basic sites, achieving a complete description of structures and binding interactions using X-ray diffraction techniques is not feasible due to structural and compositional heterogeneities. Thus, alternative techniques are required to gain insight into the nature of binding interactions between Lewis acids and π-conjugated polymer systems.

Solid-state magic-angle spinning (MAS) nuclear magnetic resonance (NMR) spectroscopy, due to its sensitivity to molecular interactions, is well-suited to probe short-range structures in heterogeneous materials. The application of solid-state NMR spectroscopy for the study of conjugated polymers has largely been centered on techniques that provide key information of different local bonding environments around each atom.[31] Information obtained from chemical shifts and dipole-dipole couplings can be translated into a description of understanding how inter- and intramolecular interactions influence three-dimensional structures. To this end, powerful 2D solid-state NMR experiments in conjunction with modelling techniques have been employed to elucidate, for example, the inter- and intramolecular interactions in poly(3-hexylthiophene),[32] perylenediimide (PDI),[33] a bithiophene derivative (TT),[34] ribbon-like self-assembly of pyrimidine base,[35] diketopyrrolo-pyrrole-dithienylthieno[3,2-*b*]thiophene (DPP-DTT),[36] and polymer:fullerence composites with different sidechain lengths and structures.[37–39]

The main objective of this work is to elucidate the binding interactions of the Lewis acid tris(pentafluorophenyl)borane (BCF) with the organic semiconductor poly[2,7-(9,9-bis(2-hexadecyl)-9*H*-fluorene)-*alt*-4,7-(9,9-dihexadecyl-9*H*-fluorene-2,7-diyl)bis[1,2,5]thiadiazolo[3,4-*c*]pyridine)] (PFPT). This polymer (Scheme 1), with a regioregularity shown in the Experimental Section, Scheme 2, was chosen due to (i) the lack of observable p-type doping upon adduct formation so that the effects of binding could be isolated from the effects of doping (Supporting Information, SI, Figure S1), and (ii) the incorporation of the [1,2,5]-thiadiazolo[3,4-*c*]pyridine (PT) acceptor moiety, which has been shown to strongly bind various Lewis acids, though it remains unclear which of the 4 Lewis basic sites participate in adduct formation (Scheme 1).[12] With a more detailed investigation of the aforementioned binding interactions, the aim of this study is to achieve a fundamental understanding of how these interactions manifest themselves in the modification of optoelectronic properties.

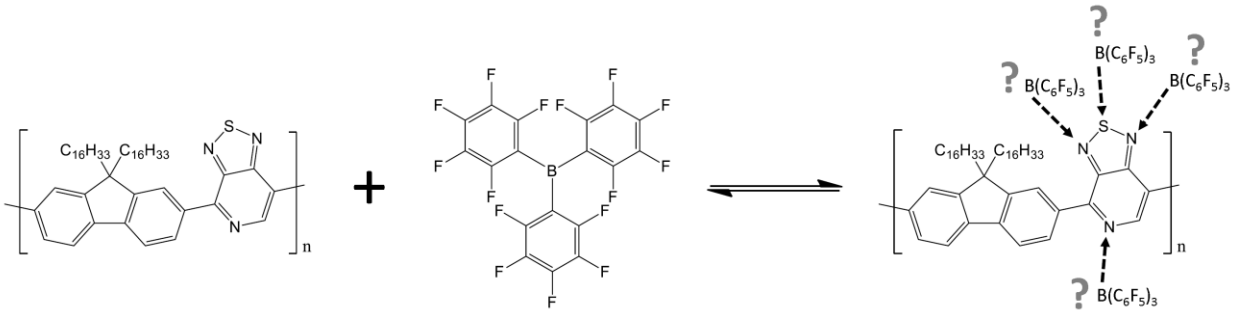

Scheme 1. Schematic representation of Lewis acid adduct formation, which is an equilibrium process with multiple potential Lewis basic binding sites on the polymer PFPT. The precise regioregular chemical structure of PFPT is detailed in the Experimental Section, Scheme 2 (simplified version shown here).

In this paper we report the synthesis of the novel PFPT polymer and its interaction with BCF in both solution and film by using a multitechnique approach that combines solution- and solid-state NMR spectroscopy, optical absorption spectroscopy, photoluminescence spectroscopy, X-ray photoelectron spectroscopy (XPS), ultraviolet photoelectron spectroscopy (UPS), and DFT calculations. Formation of the adduct is accompanied by a ~0.3 eV red-shift of the main absorption peak. Further quantitative analysis of the absorbance changes in solution with various concentrations of BCF indicate that adduct formation follows the behavior of a 1:1 binding isotherm, with binding able to occur at up to 1 BCF molecule per repeat unit of PFPT. XPS, in addition to quantum chemical calculations, indicate that BCF preferentially binds to the pyridyl nitrogen of PT. We utilize multinuclear (^{1}H, ^{13}C, ^{11}B and ^{19}F) solid-state NMR to gain atomic-level insight into the intermolecular arrangements in PFPT:BCF adducts and find that BCF molecules are intercalated between the alkyl chains of fluorene moieties in PFPT such that the boron atom of BCF is directly adjacent to the pyridyl nitrogen of the PT moiety for efficient and energetically favorable binding. Finally, results from UPS show that the bandgap reduction observed when the PFPT:BCF complex forms is primarily attributable to a reduction of the energy of the lowest unoccupied molecular orbital.

Results and Discussion:

Optical absorption and photoluminescence studies of PFPT:BCF adducts in solution and in solid state films. Upon addition of BCF to PFPT, a new, red-shifted absorption peak is observed (Figure 1a, Table 1), accompanied by a change in its bright orange color to a dull purple color. Polymer concentrations are reported relative to the single donor-acceptor repeat unit, i.e. fluorene-PT. BCF induces a 0.3 eV (~70 nm) red-shift in the maximum absorption of PFPT in both film and solution (see SI Figure S2 for film absorption). In solution, adduct formation and concomitant change of the optical properties is fully reversible by the addition of a stronger Lewis base, e.g. pyridine (Figure 1a). In solid state thin-films, the PFPT:BCF adduct was found to be relatively stable when exposed to air, despite BCF being known to be hygroscopic.[39] Specifically, over the course of 5 hours, the absorbance of the adduct peak (575 nm) decreased by only 2.8% (SI Figure S3a). After several days of exposure to air, large orange spots were visibly apparent on the otherwise purple film, indicating that BCF was no longer coordinated to a significant amount of the polymer (SI Figure S3b).

Table 1. Summary of optical properties. Errors in PLQY are the standard deviation from the mean for 3 separately prepared samples.

Optical Property	PFPT, Solution	PFPT:BCF, 1:1, Solution	PFPT, Film	PFPT:BCF, 1:1, Film
Absorbance λ_{max} (nm/eV)	503/2.46	568/2.18	507/2.44	575/2.16
E_{opt} (eV)	2.2	1.9	2.2	1.9
PL λ_{max} (nm/eV)	570/2.18	743/1.67	581/2.13	726/1.71
PLQY (%)	75±3	5.4±0.3	11.1±0.6	6.6±0.2

By analyzing how the concentration of BCF influences the absorbance of the new, red-shifted peak, we were able to determine that PFPT and BCF (in chlorobenzene solution) exhibit the behavior of a 1:1 binding isotherm. Specifically, the mole ratio plot, Figure 1b, indicates a 1:1 binding stoichiometry.[41] This suggests that (i) BCF can coordinate to every single PT unit of the polymer, and (ii) that there is only 1 binding site per repeat unit despite there being multiple Lewis basic sites. Previous studies of Lewis basic polymers suggest that BCF is unable to coordinate to every single repeat unit.[11,12] These studies also suggest that adduct formation results in a twisting of the otherwise planar polymer backbone. DFT calculations on a fluorene-PT-fluorene (F-PT-F) oligomer indicate that the PFPT backbone is already significantly twisted (SI Figure S4), and upon coordination, twists even further (SI Figure S5). Upon coordinating BCF at the pyridyl nitrogen, the F-PT dihedral angle, which is closest to the pyridyl nitrogen of PT, changes by 56° from -18° to -74°, and the other dihedral angle (PT-F, away from the pyridyl nitrogen) changes by 66° from -35° to +31°. However, the initially twisted state of the PFPT backbone may facilitate complete binding by minimizing steric interference, while also mitigating the energy penalty for breaking conjugation due to twisting of the backbone upon coordination, which may be a significant problem in polymers with planar backbone conformations. Thus, in order to maximize adduct formation, it may be advantageous to use conjugated polymers with non-planar backbones.

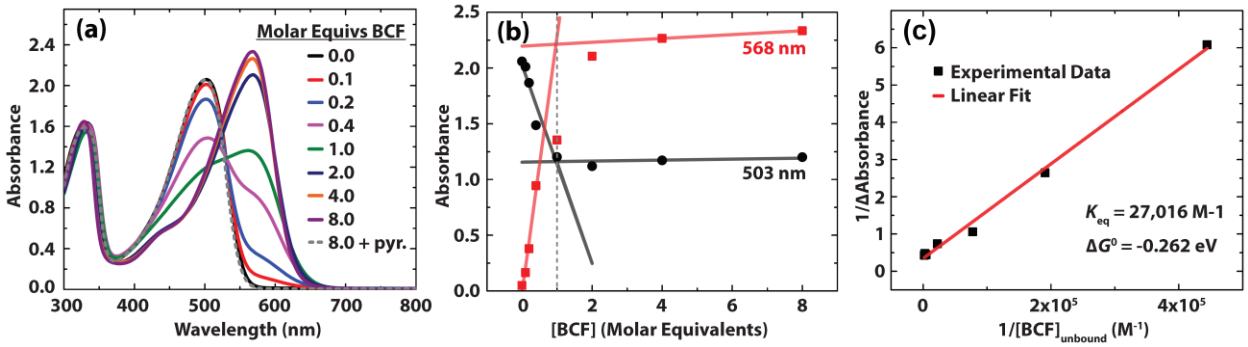

Figure 1. (a) Absorption spectra of PFPT with various amounts of BCF. (b) Absorbance of the main PFPT optical transition (503 nm) and adduct optical transition (568 nm) as a function of BCF concentration. The dashed vertical line at 1.0 molar equivalents is a guide for the eye. Solid black and red lines are linear fits to regions of high and low BCF concentrations. (c) Benesi-Hildebrand plot.

A Benesi-Hildebrand plot (Figure 1c) was constructed from the absorption data after applying a Taylor's series expansion in order to solve for the actual concentration of unbound BCF in solution (see Experimental Section for more details).[42] This analysis resulted in the determination of the equilibrium

binding constant, K_{eq}, which we found to be 27,016 M^{-1} at room temperature, corresponding to a Gibbs free energy change, $\Delta G°$, of -0.262 eV ($\Delta G^{\circ} = -k_B T ln K_{eq}$, T = 298 K and k_B = Boltzmann constant). This binding constant is 2 orders of magnitude larger than what was reported for a planar oligomer bearing the PT unit, a difference which we attribute to the relative amount of backbone deformation in the Lewis basic molecule/polymer upon binding BCF, as mentioned previously.[12] The procedure for determining these thermodynamic data from simple absorption measurements, as further detailed in the Experimental section, provides an alternative to NMR measurements, which can also be used to extract the same thermodynamic quantities (*vide infra*).

With 0.5 equivalents of BCF in solution, photoluminescence (PL) is observed from both the adduct and the pure polymer (Figure 2a), with adduct emission red-shifted from PFPT emission by about 0.5 eV (173 nm). At 1.0 equivalents of BCF the PL is dominated by adduct emission even though many binding sites are not occupied by BCF, as confirmed by optical absorption. This is clearly a result of inter and intramolecular energy transfer processes. The Stokes shift (peak to peak energy difference) of the adduct (0.5 eV, 175 nm) is large relative to the Stokes shift of PFPT itself (0.3 eV, 67 nm), indicating that the adduct undergoes significant geometrical changes while in the excited state. We suspect that these geometrical changes are also responsible for the large decrease in the photoluminescence quantum yield (PLQY) upon adduct formation, as shown in Table 1. These observations are consistent with the 'loose bolt' or 'free rotor' effect, which are known to enhance nonradiative decay pathways.[43] In fact, we observed the lifetime of the adduct at 0.5 and 1.0 molar equivalents to be shorter than the lifetime of the polymer by itself (SI Figure S6).

Interestingly, upon addition of 2.0 equivalents of BCF, the PL maximum blue-shifts relative to the lower BCF concentrations, and the lifetime increases slightly. We attribute this trend to a twisting of the PFPT backbone upon complete coordination of BCF, which then inhibits further geometric relaxation in the excited state. In polymers with only partial coordination of BCF, i.e. at concentrations of 0.5 and 1.0 equivalents, the unbound FPT moieties, together with adduct chain segments, are able to undergo a more favorable geometric relaxation in the excited state, resulting in the observed red-shifted emission. Because the adduct absorption peak wavelength does not significantly change with differing concentrations of BCF, the underlying cause of the blue shifting PL with increasing BCF concentration must be related to the polymer:Lewis acid excited state properties.

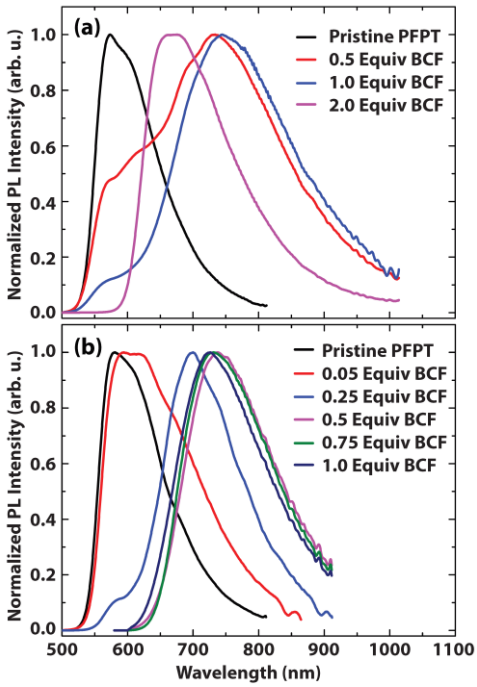

Figure 2. Photoluminescence of PFPT with various concentrations of BCF (a) in chlorobenzene and (b) as solid-state thin films.

The PL of pure PFPT in the solid state (Figure 2b) is similar to its PL in solution, although the PLQY of thin films (11%) is lower than the PLQY in solution (75%). From PLQY and lifetime measurements we were able to calculate the radiative and nonradiative decay rates in film and solution for the pure polymer (SI Table S1). The rate of radiative decay was comparable in film and solution, but the rate of nonradiative decay in the solid state was one order of magnitude larger than in solution. Thus, it is likely that in the solid state, where intermolecular energy transfer processes are enhanced due to short intermolecular distances, rapid energy transfer to defect sites and impurities is responsible for the decrease in PLQY.[44]

The PL maximum of thin films with BCF is red-shifted from the PL maximum of pure PFPT films by about 0.4 eV, or 145 nm (Table 1). The Stokes shift of the adduct (0.5 eV, 151 nm) is greater than that of pure PFPT (0.3 eV, 74 nm), not unlike the results in solution. However, in contrast to what is observed in solution, the adduct PL lifetimes are longer than the PL lifetime of neat PFPT (SI Figure S7). From a theoretical standpoint (Einstein's coefficient of spontaneous emission and the Strickler-Berg relationship), one would typically expect that a decrease in the optical transition energy would be concomitant with an increase in the natural lifetime (decrease in the rate of radiative decay).[43] In the solution phase an increase in lifetime is not observed due to significant nonradiative decay, as evidenced by the large decrease in PLQY. Furthermore, the PL maximum in the solid state red-shifts with increasing concentration of BCF up until about 0.75 equivalents, after which there is only a very slight blue-shift. These photoluminescence results are consistent with the restricted motion expected in solid-state films as compared to solution, which considerably weakens the impact of the free rotor and loose bolt effects, as well as excited-state geometric relaxation effects. Despite these differences, the PLQY of the PFPT:BCF 1:1 adduct in the solid state is still low, 6.6%, similar to the adduct PLQY in solution, 5.4%. Concerning adduct formation with polyfluorene-based polymers and BCF, Zalar et al. observed an increase in the PLQY of thin films, whereas Lin et al. observed a decrease in the PLQY of thin films.[16,17] While molecular packing is known to have

significant effects on solid-state PLQY, the relative strength of the B-N bond and the local environment of the adduct may also play a role; therefore, it is important to gain insight into the intermolecular interactions between the PFPT and BCF.

Atomic-level insight into compositions and structures of PFPT:BCF adducts. The formation of PFPT:BCF adduct in chloroform was investigated via ^{11}B NMR spectroscopy. In particular, ^{11}B chemical shifts are expected to be sensitive to changes in the chemical bonding environments such that tri- and tetracoordinated boron atoms can be identified and distinguished.[45,46] As shown in Figure 3a,b, a significant displacement in the isotropic ^{11}B chemical shift occurs upon adduct formation, as compared to the ^{11}B chemical shifts of neat BCF, which can be attributed to the change in the bonding environment of the central boron atom. This observation is exemplified by geometrical changes around the boron atom in the optimized DFT structures of bound and unbound BCF, as shown in Figure 3a,b, respectively.[47] Notably, the boron atom in unbound (3-coordinate sp^2) BCF adopts a trigonal planar geometry ($\delta \approx 56$ ppm). By comparison, the same boron atom in the adduct (4-coordinate sp^3) adopts a more tetrahedral-like geometry, which has a much different chemical shift ($\delta \approx -3$ ppm). By comparing the relative integrals of bound and unbound BCF in a solution of PFPT with 1.0 molar equivalents of BCF, we determined an equilibrium binding constant of 21,000 M^{-1} which is in excellent agreement with the optical absorbance results and analyses. The relative integration also indicates that 95% of PT moieties on PFPT are bound to BCF. Moreover, the presence of only one peak near 0 ppm suggests that there is only a single preferred Lewis basic binding site in the polymer. When BCF was added to 4,7-dibromobenzo[*c*]-1,2,5-thiadiazole, no tetracoordinate boron was observed by ^{11}B NMR, suggesting that azole nitrogen atoms and sulfur atoms are either not sufficiently Lewis basic, or too sterically crowded, to result in adduct formation (SI Figure S8).

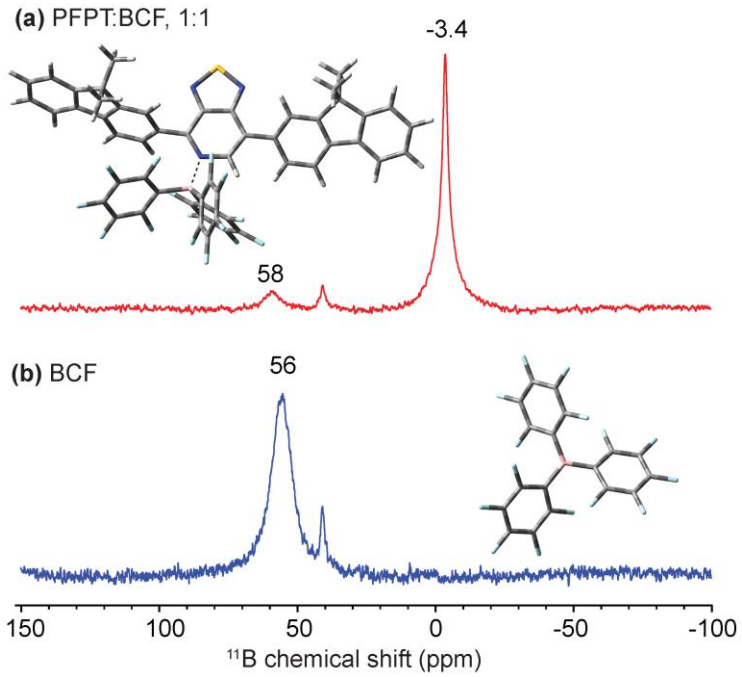

Figure 3. Solution-state ^{11}B NMR spectra acquired at 11.7 T and at room temperature of (a) PFPT with 1.0 molar equivalents of BCF and (b) neat BCF. The displacement of the ^{11}B signal is characteristic of the change in the local bonding environment of the boron atom. DFT optimized structures are also depicted.

DFT calculations were employed to probe the binding site of BCF on the PFPT backbone by assessing the relative change in internal energy ($\Delta U°$) of a F-PT-F oligomer upon coordination to different Lewis basic sites, temperature effects excluded (see SI for more details). For binding at the azole nitrogen atoms of the PT moiety, $\Delta U°$ is positive. In contrast, for binding at the pyridyl nitrogen atom of PT, $\Delta U°$ is -0.08 eV. Attempts to force BCF to bind at the sulfur atom were unsuccessful. Thus, our calculations suggested that the pyridyl nitrogen atom of PT is the most likely position for BCF binding.

Thin films of PFPT and a 1:1 complex with BCF were also investigated by XPS (SI Figure S13). Both pristine PFPT and PFPT with 1.0 equivalents of BCF have identical sulfur *2p* doublet peaks, indicating that there is no significant interaction of the Lewis acid with the sulfur atom on the PT moiety. Pristine PFPT exhibits two nitrogen *1s* peaks, as shown in Figure 4, with peak areas corresponding to a ratio of approximately 2:1. This suggests that the larger peak at higher binding energy (400.1 eV) corresponds to the azole nitrogen atoms, whereas the smaller peak at lower binding energy (399.2 eV) corresponds to the pyridyl nitrogen atom.[48,49] Upon addition of 1.0 equivalents of BCF, a new nitrogen *1s* peak at higher binding energy (401.1 eV) is observed. Importantly, the relative area of the azole nitrogen peak, compared to the total area of the combined nitrogen peaks, does not change (Table 2). However, the peak corresponding to the pyridyl nitrogen atom is considerably reduced relative to the total area of nitrogen *1s* peaks. These results indicate that BCF is interacting primarily with the pyridyl nitrogen atom of PT, and not the other Lewis basic sites. Because BCF is a Lewis acid, it withdraws electron density from the pyridyl nitrogen atom, making it overall more electron poor and, therefore, causing the new adduct peak to occur at higher binding energy, a shift of 1.9 eV.

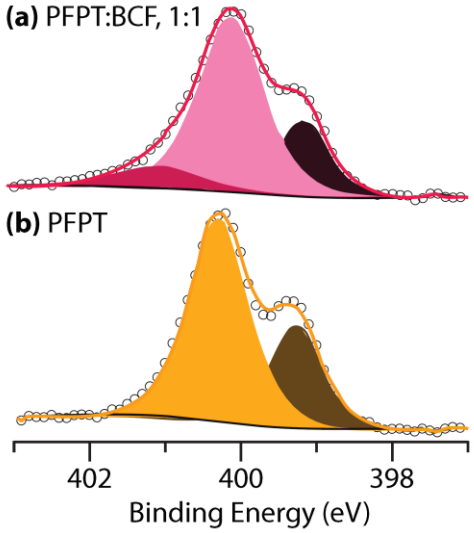

Figure 4. High-resolution XPS spectra of N *1s* for thin films of (a) PFPT with 1.0 molar equivalents of BCF and (b) neat PFPT.

Table 2. Peak percentages from Voigt fits to N *1s* high-resolution XPS spectra.

Binding Energy	PFPT	PFPT:BCF, 1:1
399.2 eV	30 %	22 %
400.1 eV	70 %	68 %
401.1 eV	--	10 %

The impact of BCF on the morphology of PFPT in the solid-state was probed by grazing-incidence wide-angle X-ray scattering (GIWAXS) and atomic force microscopy (AFM). As shown in SI Figure S14, the surface roughness of PFPT films do not change considerably upon addition of BCF. The root-mean-square surface roughness of pristine PFPT is 0.51 nm and increases only slightly to 0.56 nm upon addition of 0.10 molar equivalents BCF. GIWAXS data (SI Figure S15) show that pristine PFPT is rather amorphous and that there are no discernable changes in the GIWAXS diffraction pattern with up to 0.10 molar equivalents BCF. We investigated how the addition of BCF impacts the conductivity of PFPT films, but the conductivity of PFPT was found to be too low to make any conclusions (SI Figure S16). At room temperature, the conductivities of PFPT and PFPT with 0.10 molar equivalents BCF were below the limit of detection, precluding further electrical measurements.

To gain molecular-level insight into the local structures of the PFPT:BCF adducts in the solid state, multinuclear MAS-NMR spectra were acquired and analyzed. The analyses of isotropic ^{1}H, ^{13}C, ^{19}F and ^{11}B NMR chemical shifts are expected to provide information on local bonding environments in BCF and PFPT. For example, the one-dimensional (1D) solid-state^{11}B MAS NMR spectrum of a 1:1 PFPT:BCF complex in Figure 5a exhibits a signal at -1.8 ppm, which is characteristic of tetrahedrally coordinated boron atoms and is consistent with the solution-state ^{11}B NMR spectrum of the PFPT:BCF complex. While this reflects bonding interactions between BCF and PFPT moieties, the ^{11}B MAS NMR spectrum provides little specific information concerning the intermolecular structure(s) or binding sites of PFPT:BCF complexes. Although ^{1}H MAS NMR spectroscopy benefits from the high sensitivity associated with ^{1}H nuclei (100% natural abundance) that can be used to characterize conjugated backbone moieties in PFPT and BCF, such spectra often suffer from considerably lower spectral resolution.

Complementary insights on the local bonding environments of ^{13}C moieties in PFPT:BCF adducts can be obtained by analyzing solid-state 1D $^{13}C\{^{1}H\}$ and $^{13}C\{^{19}F\}$ CP-MAS spectra. Such analyses exploit the enhancement of certain ^{13}C signal intensities that are increased by transfer of ^{1}H or ^{19}F spin-polarization, according to the strengths of their ^{1}H-^{13}C or ^{19}F-^{13}C dipole-dipole couplings, from specific BCF and PFPT aromatic carbon moieties. This enables distinct local C-H and C-F environments to be resolved and identified. For example, a comparison of the 1D $^{13}C\{^{1}H\}$ and $^{13}C\{^{19}F\}$ CP-MAS NMR spectra in Figure 5 shows ^{13}C signals with different intensities that are associated with different BCF and PFPT moieties of the complex. In particular, the analyses of the $^{13}C\{^{1}H\}$ and $^{13}C\{^{19}F\}$ CP signal enhancements associated with the ^{13}C site adjacent to the pyridyl nitrogen atom (shown in green in the schematic diagram in Figure 5a) enabled the intramolecular ^{13}C-^{1}H interactions in PFPT and the intermolecular ^{13}C-^{19}F interactions between PFPT and BCF moieties in the PFPT:BCF complex to be separately identified and distinguished. In the 1D $^{13}C\{^{1}H\}$ CP-MAS spectrum (Figure 5b), the partially-resolved signal at 123 ppm in the aromatic region is associated with the carbon atom (green) bearing a proton next to the pyridyl nitrogen atom of PFPT. The broad intensity distribution centered at 129 ppm corresponds to aromatic carbon atoms (red, cyan, and purple) that are directly bonded to protons in fluorene moieties. The relatively weak ^{13}C signals in the range 133-150 ppm are attributed to the overlapping contributions from carbon atoms (black) in the BCF moieties, which while not directly bonded to hydrogen atoms, are nevertheless within 1 nm. The relatively narrow ^{13}C signal at 153 ppm is assigned to the six carbon atoms (grey) of the FPT moieties. Further insights were obtained from the 1D $^{13}C\{^{19}F\}$ CP-MAS spectrum (Figure 5c), in which partially resolved ^{13}C signals in the ranges 145-150 and 132-138 ppm are enhanced by ^{19}F nuclei that are directly bonded to the carbon atoms (black) in the BCF moieties. Interestingly, the ^{13}C signal at 123 ppm associated with the carbon atom (green) adjacent to the pyridyl nitrogen in the FPT moiety is also relatively enhanced by ^{19}F spin-polarization, which indicates its nanoscale proximity to the fluorine atoms in C_6F_5 units. Together, the

$^{13}C\{^{1}H\}$ and $^{13}C\{^{19}F\}$ analyses enable the intramolecular C-H and intermolecular C-F interactions to be distinguished in the PFPT:BCF complex, further supported by the analyses of 2D $^{1}H\{^{1}H\}$ and $^{1}H\{^{19}F\}$ NMR spectra discussed below.

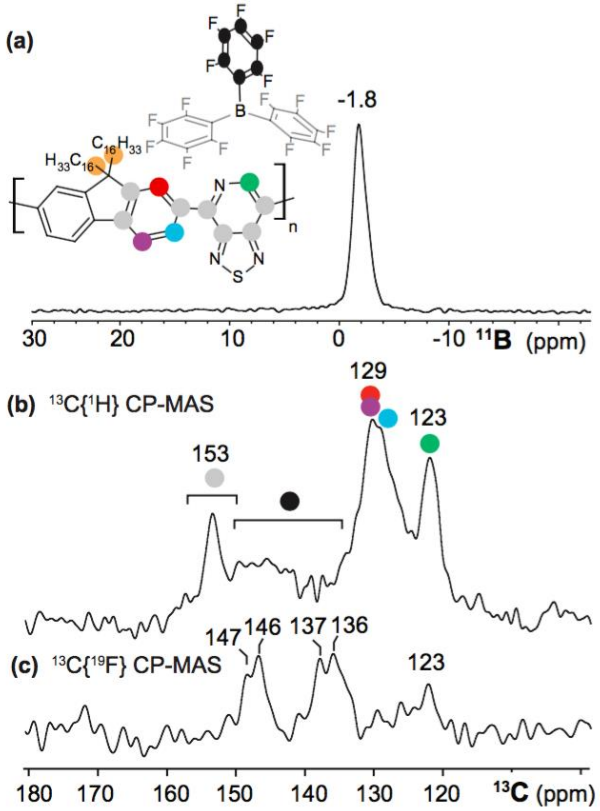

Figure 5. Solid-state 1D NMR spectra of PFPT:BCF complex acquired at 298 K, 9.4 T, and 15 kHz MAS. (a) Single-pulse ^{11}B MAS NMR spectrum with the signal at -1.8 ppm assigned to tetrahedrally coordinated boron atoms in PFPT:BCF. (b) $^{13}C\{^{1}H\}$ and (c) $^{13}C\{^{19}F\}$ CP-MAS NMR spectra acquired using 2 ms of CP contact time. The color code depicts assignments of ^{13}C atoms in the BCF and PFPT moieties according to the schematic structural diagram of the PFPT:BCF complex in (a).

Molecularly proximate and dipole-dipole-coupled spin pairs within approximately 1 nm can be probed by using solid-state two-dimensional (2D) NMR techniques, enabling intermolecular ^{19}F-^{1}H interactions between BCF and PFPT to be identified and elucidated.[31,36,50–53] For example, a rotor-synchronized 2D dipolar-mediated $^{1}H\{^{19}F\}$ heteronuclear multiple-quantum correlation (HMQC) spectrum acquired using 0.32 ms of recoupling time is shown in Figure 6a, accompanied by 1D ^{1}H MAS and 1D ^{19}F MAS spectra along the top horizontal axis and the left vertical axis, respectively. The relatively broad distribution of intensity centered at -133 ppm corresponds to ^{19}F moieties in the *ortho* position of the C_6F_5 moieties in BCF, while partially resolved ^{19}F signals in the range -158 to -163 ppm correspond to fluorine atoms in *para* and *meta* positions. These assignments are consistent with the isotropic ^{19}F chemical shifts of aromatic groups reported in the literature.[54] In the solid-state 2D $^{1}H\{^{19}F\}$ HMQC NMR spectrum of Figure 6a, intensity correlations are observed between ^{1}H signals at 8.2 ppm (aromatic groups of PFPT) and 1.1 ppm (branched alkyl sidechains of PFPT) with the ^{19}F signals at -163 and -158 ppm from the *meta* and *para* ^{19}F atoms in BCF, which establish the close spatial proximities of these PFPT and C_6F_5 moieties. In contrast, no such correlated intensity is observed between aromatic ^{1}H signals of PFPT and the *ortho* ^{19}F signal of C_6F_5 moieties (-133 ppm), reflecting weaker ^{19}F-^{1}H dipole-dipole interactions between the PFPT

backbone and sidechain ^{1}H moieties. These 2D intensity correlations are consistent with the formation of a polymer:Lewis acid adduct in which BCF molecules bind near the pyridyl nitrogen atoms of PFPT.

Complementary insights on the inter- and intramolecular ^{1}H-^{1}H interactions of PFPT polymer chains in the presence of BCF are obtained from the 2D $^{1}H\{^{1}H\}$ DQ–SQ spectra. In Figure 6b, the left vertical dimension shows the ^{1}H double-quantum (DQ) chemical shifts at the sum of the respective single-quantum (SQ) chemical shifts for dipole-dipole-coupled ^{1}H spin pairs within a distance of approximately 0.5 nm. For example, intensity at a ^{1}H SQ chemical shift of 1.1 ppm and a ^{1}H DQ chemical shift of 1.1 + 1.1 = 2.2 ppm, originates from adjacent ^{1}H moieties in the methyl and methylene groups of the hexadecylalkyl chains. In addition, off-diagonal intensity correlations at ^{1}H SQ chemical shifts of 1.1 and 8.2 ppm and a ^{1}H DQ chemical shift of 1.1 + 8.2 = 9.3 ppm reflect the intramolecular proximities of the hexadecylalkyl chains and aromatic ^{1}H atoms in the fluorene moieties of PFPT. As expected, no such DQ-SQ intensity is observed for ^{1}H nuclei adjacent to the pyridyl nitrogen atoms and ^{1}H nuclei in the alkyl sidechains attached to the fluorene moieties. Additional self-correlated intensity at a ^{1}H SQ chemical shift of 8.3 ppm and a ^{1}H DQ chemical shift, 8.2 + 8.2 = 16.4 ppm indicates the closer through-space proximity of ^{1}H moieties in the aromatic fluorene and PT moieties of PFPT. The combined 2D $^{1}H\{^{19}F\}$ and $^{1}H\{^{1}H\}$ NMR analyses thus provide direct evidence of the spatial proximities of BCF and PFPT, and indicate that the BCF molecules are preferentially located between the branched $C_{16}H_{33}$ sidechains and that the boron atoms of BCF interact with the pyridyl nitrogen atoms of PFPT.

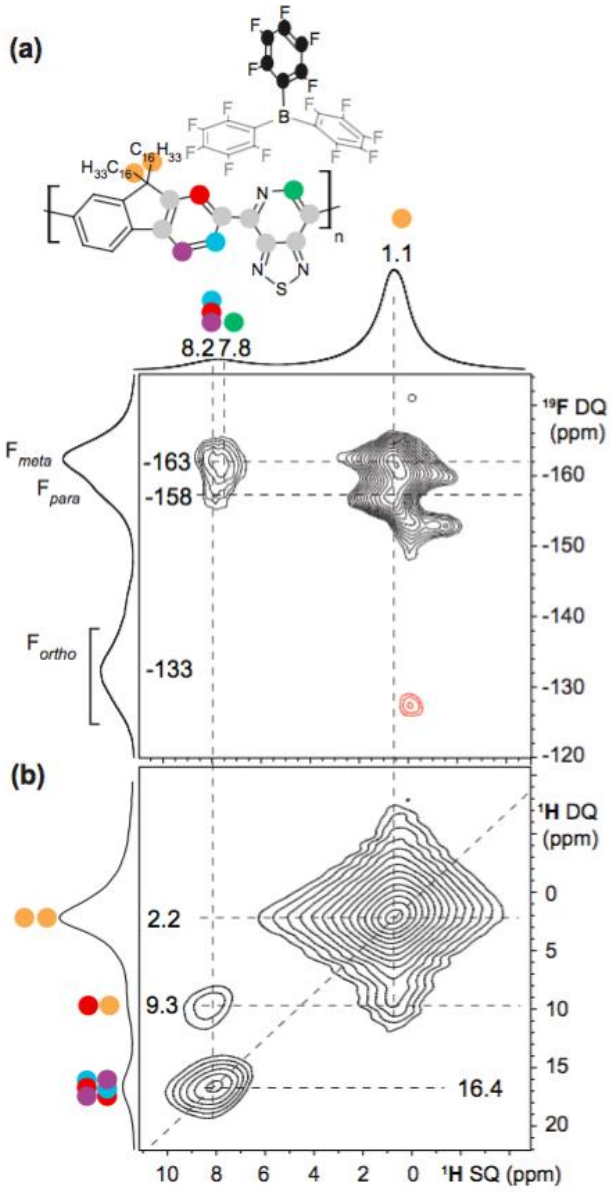

Figure 6. (a) A solid-state 2D ^{1}H{^{19}F} HMQC NMR spectrum of a 1:1 PFPT:BCF complex (schematic structure shown) with 1D ^{1}H and ^{19}F MAS NMR spectra along the horizontal and vertical axes, respectively, for comparison. The spectrum was acquired at 298 K, 9.4 T, and 25 kHz MAS with a recoupling time of 0.32 ms. (b) A solid-state 2D ^{1}H{^{1}H} DQ-SQ NMR spectrum acquired for the same complex under similar conditions, except for the recoupling time was 40 μs, plotted with a double-quantum projection on the vertical dimension. The color code depicts the assignment of ^{19}F and ^{1}H signals associated with the BCF and PFPT species, as depicted also in the schematic structural diagram.

Understanding bandgap engineering using time-dependent DFT modelling and ultraviolet photoelectron spectroscopy. With a detailed physical description of the nature of Lewis acid binding, we next investigated the solid-state electronic properties via UPS. The ionization potential (IP) of PFPT, -6.05 eV, became slightly deeper when 1.0 equivalents of BCF was added, resulting in an ionization potential of -6.15 eV (SI Figure S17). Assuming that the exciton binding energy of the adduct is similar to that of pristine PFPT, the

change in electron affinity (EA) is then given by the sum of changes in the IP and E_{opt}.[55,56] From the IP dropping by 0.1 eV and the optical bandgap decreasing by 0.3 eV, we can thus infer that the EA of the adduct decreases by 0.4 eV relative to pristine PFPT. These measurements elucidate a detailed picture of how frontier molecular orbitals change upon adduct formation, which is depicted in Figure 7.

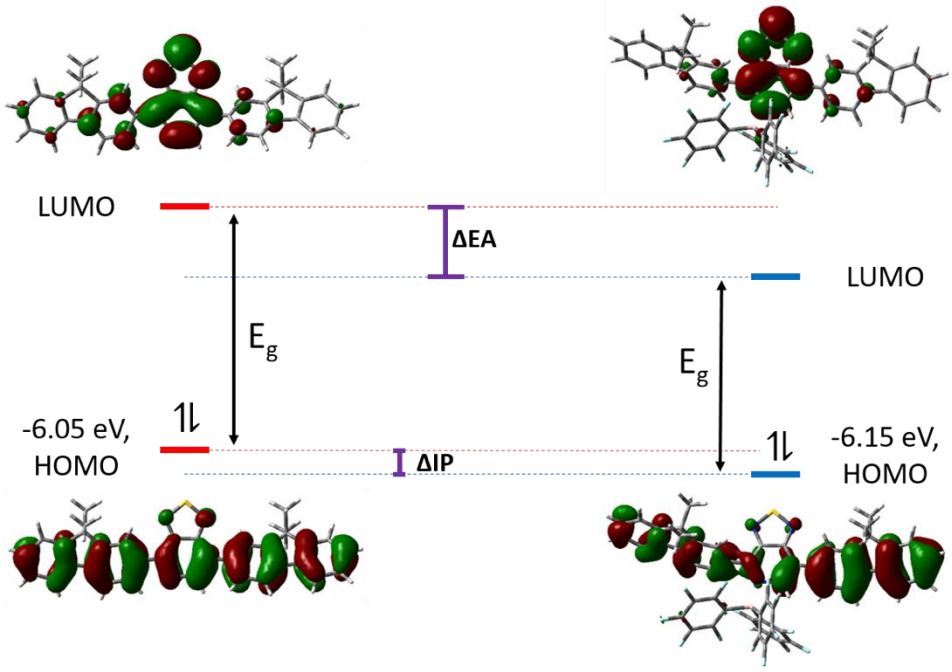

Figure 7. Energy diagram of how adduct formation changes the energy of molecular orbitals, accompanied by TD-DFT calculations which show the relevant wavefunctions. Experimental values of HOMO energies, as determined by UPS of thin films. The relative change in the LUMO energy, i.e. ΔEA, upon adduct formation is inferred by the experimentally determined change in HOMO energies, ΔIP, and reduction of the optical bandgap, E_{opt}, while assuming that the change in exciton binding energy upon adduct formation is negligible.

Time-dependent (TD) DFT calculations, carried out on an F-PT-F oligomer, provide further insight into why the LUMO energy is reduced significantly more than the HOMO energy upon coordination with BCF. The oligomer, by itself, has a HOMO wavefunction that is well delocalized on the conjugated backbone, but a LUMO that is localized on the PT acceptor moiety, demonstrating ICT character, as is expected for D-A molecules and polymers. Upon coordination of BCF to the pyridyl nitrogen, the HOMO is relatively unaffected, although a very small portion of the wavefunction does extend onto aromatic rings of BCF. Thus, it is not surprising that by UPS we observed only a small reduction in IP upon adduct formation. However, the LUMO wavefunction, upon binding the Lewis acid, noticeably extends onto BCF, while simultaneously retracting from the neighboring fluorene moieties. This is clearly associated with the Lewis acid withdrawing electron density from the LUMO, which results in a significant stabilization (reduction) of the LUMO energy.

Conclusion:

To summarize, this in-depth study reveals how the Lewis acid $B(C_6F_5)_3$ can be used for post-synthesis bandgap engineering in a model Lewis basic polymer, PFPT. UPS measurements and TD-DFT calculations show that the reduction in the optical bandgap (ΔE_{opt} = 0.3 eV) can be attributed primarily to $B(C_6F_5)_3$ withdrawing electron density from the LUMO of PFPT, resulting in a significant decrease of the LUMO energy of the PFPT:BCF adduct. A combination of XPS, solution- and solid-state multinuclear NMR, and DFT calculations show that, although PFPT has multiple Lewis basic sites which could potentially bind $B(C_6F_5)_3$, it is only the pyridyl nitrogen which forms the adduct. Importantly, solid-state 1D ^{11}B, $^{13}C\{^1H\}$ CP-MAS and $^{13}C\{^{19}F\}$ CP-MAS and 2D $^1H\{^{19}F\}$ and $^1H\{^1H\}$ correlation NMR analyses provide evidence that BCF molecules are intercalated between branched alkyl sidechains of PFPT and that the boron atoms of BCF interact with the pyridyl nitrogen atoms of PFPT. In particular, the relative $^{13}C\{^1H\}$ and $^{13}C\{^{19}F\}$ CP signal enhancements observed for the ^{13}C sites adjacent to the pyridyl nitrogen atoms of PFPT indicate the mutual nanoscale proximities of the BCF and PFPT moieties. These results are corroborated by the 2D $^1H\{^{19}F\}$ correlation NMR measurements and analyses, which establish the ^1H and ^{19}F proximities in PFPT:BCF complex at sub-nm to nm distances. In addition, analysis of spectroscopic data reveals that adduct formation in solution is an equilibrium process, specifically, a 1:1 binding isotherm, with the equilibrium strongly favoring adduct formation ($\Delta G°$ < -0.2 eV). This detailed investigation also highlights the important role of the steric conformation of the polymer backbone, which in the case of PFPT, because of its non-planar structure, is able to bind one $B(C_6F_5)_3$ molecule for every repeat unit of PFPT.

Molecular-level and atomic-level insights into the structure and optical properties of Lewis acid adducts that form with Lewis basic polymers, as acquired in this study, are expected to guide the development of new polymers which are compatible with bandgap engineering via Lewis acid adduct formation, which is of broad interest to the organic semiconductor community. This general strategy may be used not only for tailoring the optical properties of polymer light-emitting diodes (PLEDs) and organic photovoltaics (OPVs), but also for the fine-tuning of energy levels, post-synthesis. In PLEDs and field-effect transistors, modifying the HOMO and LUMO energies may beneficially enhance (or inhibit) charge injection as well as tune the optical band gap, whereas in OPVs, energy level alignment between an electron acceptor material and electron donor material is critical for achieving efficient charge separation and high open-circuit voltage.[57–62]

Experimental:

BCF was purchased from Tokyo Chemical Industry in the purity greater than 98% and used as received. Because BCF is very hygroscopic, we regularly assessed contamination of water by dissolving some BCF in a dry NMR solvent and looking for any proton peaks other than what is expected from the solvent. Storage and handling of BCF in nitrogen atmosphere gloveboxes was sufficient to prevent water contamination. All solvents were purchased dry. Molecular sieve was added to these solvents before use. All measurements and sample preparation were carried out in oxygen-free environments. All solutions were allowed to equilibrate at room temperature overnight, or longer, before measurements were obtained or films prepared.

The regioregular PFPT was synthesized in a four step procedure starting from 2,7-dibromo-9*H*-fluorene. A more complete description of the synthesis, and characterization details, can be found in the SI.

After alkylation with 1-bromohexadecane and stannylation *via* lithium-bromine exchange (9,9-dihexadecyl-9*H*-fluorene-2,7-diyl)bis(trimethylstannane) (M1), was yielded in 82%. To receive a regioregular polymer M1 was converted in a *Stille* coupling with an excess of 4,7-dibromo-[1,2,5]thiadiazolo[3,4-*c*]pyridine to 4,4'-(9,9-dihexadecyl-9*H*-fluorene-2,7-diyl)bis(7-bromo-[1,2,5]thiadiazolo[3,4-*c*]pyridine) (M2). Because of the higher reactivity of the C–Br in α-position to the pyridine nitrogen full regioselectivity was achieved.[63] The polymerization of M1 and M2 was performed under microwave condition at 200 °C for 80 min. For endcapping with phenyl units the received polymer was transformed via *Stille* coupling with tributylphenylstannane and phenylbromide, respectively.

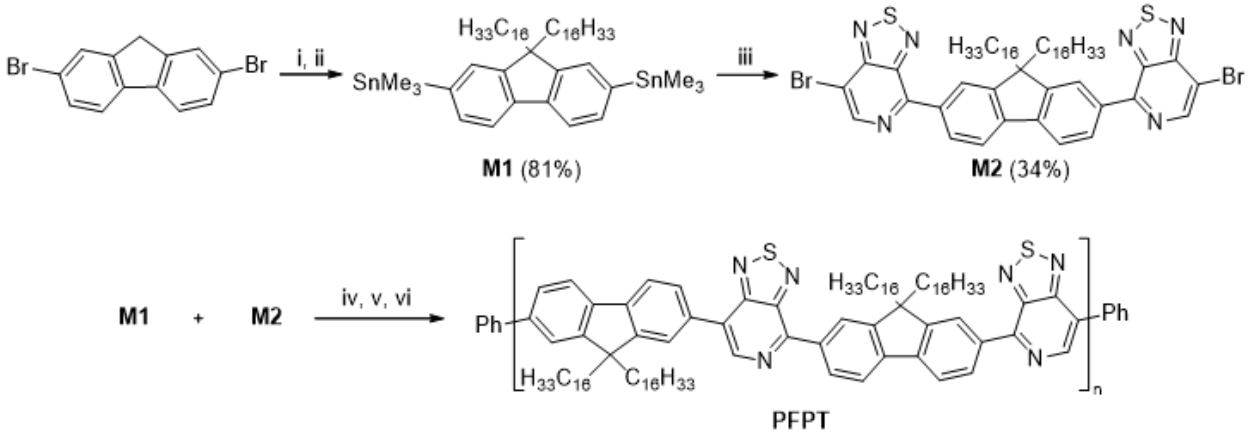

Scheme 2. Synthesis of PFPT: (i) KO*t*Bu, 1-bromohexadecane, THF, 40 °C, 40 h; (ii) *t*BuLi, Bu_3SnCl, THF, -78 °C → rt; (iii) 4,7-dibromo-[1,2,5]thiadiazolo[3,4-*c*]pyridine, $Pd(PPh_3)_4$, toluene, 120 °C, 22 h; (iv) $Pd(PPh_3)_4$, xylene/DMF, MW, 200 °C, 80 °C; (v) $PhSnBu_3$, $Pd(PPh_3)_4$, 160 °C, 50 min; (vi) PhBr, $Pd(PPh_3)_4$, 160 °C, 50 min.

Thin films used for absorption and fluorescence spectroscopy were spun-coat (800 rpm) onto clean glass substrates from solutions in chloroform where the concentration of the polymer was approximately 20 mg/mL. They were then encapsulated using epoxy and another clean glass substrate to exclude the presence of oxygen, after which measurements were performed outside of the glovebox. For solution measurements samples were prepared inside a nitrogen atmosphere glovebox, loaded into a custom made cuvette with Teflon seal, sealed, and then brought out of the glovebox for measurements. Absorption measurements were performed on a Lambda 750 UV-Vis/NIR Spectrophotometer. The optical bandgaps (E_{opt}) were determined by the onset of absorption. A charge-coupled device camera (Princeton Instruments Pixis: 400) was used to obtain steady-state fluorescence spectra. A blackbody light source was used for spectral calibration of the detector. The photoluminescence quantum yields in solution (λ_{exc} = 503 nm) were determined in the usual way by reference to a standard dye, in this case, Rhodamine B.[64] The photoluminescence quantum yields in the solid state were determined using an integrating sphere and excitation wavelength of 458 nm.[65]

The Benesi-Hildebrand equation for a 1:1 complex is given by

$$\frac{b}{\Delta A} = \frac{1}{S_t K_{eq} \Delta\varepsilon [L]} + \frac{1}{\Delta\varepsilon S_t} \quad (1)$$

where b is the path length of the cuvette, S_t is the total substrate concentration, i.e. initial polymer repeat unit concentration, $[L]$ is the concentration of the unbound ligand at equilibrium, i.e. unbound BCF, ΔA is the change in absorbance at a defined wavelength for a particular ligand concentration (with respect to the

free substrate), $\Delta\varepsilon$ is the difference in molar absorptivity at the defined wavelength between the bound and unbound complex, and K_{eq} is the equilibrium constant for ligand binding. To use this equation, however, we must first determine [L] at equilibrium after adding a given amount of the ligand to solution. For a 1:1 binding isotherm model, mass balance of the ligand tells us that

$$L_t = [L] + [SL] = [L] + \frac{S_t K_{eq}[L]}{1 + K_{eq}[L]} \tag{2}$$

where L_t is the total ligand concentration and $[SL]$ is the concentration of the bound complex at equilibrium. A Taylor's series expansion of L_t is

$$L_t = g(L_t) + g'(L_t)([L] - L_t) + \frac{g''(L_t)}{2}([L] - L_t)^2 \cdots \tag{3}$$

where $g(L_t)$ is Equation 2, $g'(L_t)$ is $dL_t/d[L]$ and $g''(L_t)$ is $d^2L_t/d[L]^2$. Truncating at the linear term of Equation 3 and solving for $[L]$, we find a solution in the form of

$$[L] = L_t - \frac{\left(\frac{K_{eq}S_tL_t}{1 + K_{eq}L_t}\right)}{\left(1 + \frac{K_{eq}S_t}{1 + 2K_{eq}L_t - K_{eq}^2L_t^2}\right)} \tag{4}$$

For each concentration of L_t for which absorbance was measured, $[L]$ was determined by an initial guess of K_{eq} in Equation 4. Then, a Benesi-Hildebrand plot was constructed, and from the slope and intercept of the resulting linear fit, another value of K_{eq} was extracted. The initial guess in Equation 4 was modified until the K_{eq} determined from the Benesi-Hildebrand plot was equivalent to the initial guess, which finally results in our reported value of K_{eq} for BCF binding to PFPT. See reference 42 for more details.

For solution-state NMR, samples were measured using quartz NMR tubes with a specially designed Teflon screw-cap seal. Samples were loaded into the NMR tube inside the nitrogen atmosphere glovebox and sealed, then brought outside the glovebox for measuring. Deuterated chloroform was chosen due it being readily available, it being significantly cheaper than deuterated chlorobenzene, and improved solubility of the polymer in chloroform over chlorobenzene. Measurements were carried out on an Agilent Technologies 400 MHz, 400-MR DD2 Spectrometer. Proton chemical shifts are referenced to the proton peaks of residual chloroform in the bulk chloroform-d solvent. ^{11}B chemical shifts are reported relative to $\delta = 0.0$ for boron trifluoride diethyl etherate. In all experiments the concentration of the polymer (with respect to the repeat unit) and/or BCF were 20 mM. For determining the equilibrium constant, the integrated peaks of interest and initial concentrations were used to determine the precise equilibrium concentrations of adduct, [PFPT···BCF], free polymer [PFPT], and unbound BCF [BCF]. Then, the following equation was used to determine the equilibrium constant:

$$K_{eq} = \frac{[PFPT \cdots BCF]}{[PFPT] \times [BCF]}$$

in accordance with the reaction stoichiometry:

$$PFPT + BCF \leftrightarrow PFPT \cdots BCF$$

For solid-state NMR, samples were prepared by first creating a solution (where the concentration of the polymer was approximately 20 mg/mL in chloroform) in a clean 20 mL vial. Then, the solvent was allowed to evaporate in the nitrogen atmosphere glovebox. The material was scraped off the walls of the

vial and the powder was transferred into an air-tight rotor for subsequent measurements in a glove box. PFPT:BCF complex was packed into a 2.5 mm (outer diameter) zirconia rotor fitted with a Vespel® cap. The purity of the PFPT:BCF complex is reflected in the ^{1}H MAS NMR spectrum shown in Figure 6a, which is free from solvent ^{1}H signals. All solid-state MAS NMR spectra were acquired on a 9.4 T Bruker AVANCE-III NMR spectrometer equipped with 2.5 mm H-F-X probehead and Bruker variable temperature (VT) control unit. Single-pulse ^{19}F MAS NMR spectra were acquired under 25 kHz MAS conditions using 256 co-added transitions and a T_1 relaxation delay of 20 seconds, corresponding to a total experimental time of 1.5 h. Single-pulse ^{1}H MAS NMR experiments were acquired by co-addition of 32 transients with a relaxation delay of 3 s, corresponding to a total experimental time of 2 minutes. 1D $^{13}C\{^{1}H\}$ and $^{13}C\{^{19}F\}$ CP-MAS spectra were acquired under 15 kHz MAS conditions using a CP contact time of 2 ms each. Cross polarization involves the simultaneous excitation of $^{1}H/^{19}F$ and ^{13}C nuclei to enhance the signals of the latter. The ^{13}C 90º pulse duration was 4.0 µs and the ^{1}H nutation frequency was 100 kHz. 2048 co-added transients using a 3 s recycle delay, heteronuclear decoupling was applied during acquisition using SPINAL64 sequence, corresponding to a total experimental time of 2 h.[66] 2D $^{1}H\{^{19}F\}$ heteronuclear multiple-quantum coherence (HMQC) spectrum was acquired using 0.32 ms of recoupling time. 2D spectrum was acquired using 64 t_1 increments, each with 32 co-added transients, with a rotor-synchronized t_1 increment of 40 µs, corresponding to an overall experimental time of 2 h using a 3 s recycle delay. The DQ coherences were excited and reconverted using a 16-step phase cycle that incorporates $\Delta p = \pm 2$ on the DQ excitation pulses (4 steps) and $\Delta p = \pm 1$ (4 steps) on the *z*-filter 90º pulse, where *p* is the coherence order. 2D spectrum was acquired using 128 t_1 increments, each with 16 co-added transients, using a rotor-synchronized t_1 increment of 40 µs, corresponding to an experimental time of 2 h using a 3 s recycle delay. All ^{1}H and ^{13}C experimental shifts are calibrated with respect to neat TMS using adamantane as an external reference (higher ppm ^{13}C resonance, 35.8 ppm and the ^{1}H resonance, 1.85 ppm). Solid-state ^{19}F chemical shifts of PFPT:BCF complex were calibrated to ^{19}F chemical shift of Teflon at -132 ppm which in turn calibrated using neat $CFCl_3$ (^{19}F, 0 ppm) as an external reference.

All ultraviolet photoelectron spectroscopy measurements were performed on a Kratos Axis Ultra DLD spectrometer under vacuum (10^{-7} Torr) using a He I ($h\nu$ = 21.2 eV) discharge lamp at a pass energy of 5 eV. The solutions were spun cast on top of solution cleaned indium tin oxide/glass substrates to give a film with a thickness of approximately 10 nm. The films were electrically grounded to the sample bar using nickel impregnated tape. Linear fits to baseline to extract relevant parameters performed using IGOR Pro.

All X-ray photoelectron spectroscopy measurements were performed on a Kratos Axis Ultra DLD spectrometer under vacuum (10^{-8} Torr) using monochromated x-rays produced using an aluminum source running at a potential of 14 kV. A pass energy of 20 eV was used for all high-res element sweeps. The samples were spun-cast onto cleaned conductive indium tin oxide/glass substrates. The films were mounted onto a sample bar using double-sided tape, and electrically grounded to the sample bar using nickel impregnated tape. Peak fitting was performed using WINSPEC, and atomic sensitivity factors for each element were taken into account during peak integrations.

Calculated structures were optimized by DFT using the B3LYP functional and 6-31G(d,p) basis set.[67,68] Solvent effects were considered by using the SMD solvation model (solvent = chlorobenzene). For orbital analysis (TD-DFT), single-point energy calculations were performed on the B3LYP optimized geometries using the ωB97XD functional and 6-31G(d,p) basis set.[69] The value of ω for each structure was determined after sampling a range of arbitrarily chosen values and selecting that which finally satisfied Koopman's theorem.[70]

Supporting Information:
Additional measurements and calculations include EPR, UV-Vis absorbance, photoluminescence, NMR, DFT, XPS, AFM, GIWAXS, electrical conductivity, UPS, synthesis procedure, and DFT results.

Notes:
The authors declare no competing financial interest.

Acknowledgements:

This work is supported by the U.S. Department of Energy, Office of Science, Office of Basic Energy Sciences, under Award Number DE-SC0017659. D.L. thanks the Alexander von Humboldt Foundation (Feodor Lynen Research Fellowship) for the support. S.B. thanks the Bavaria California Technology Centre (BaCaTec) for travel funds to work at UCSB. D.X.C. acknowledges the National Science Foundation Graduate Research Fellowship Program under Grant No. 1650114. We acknowledge support from the Center for Scientific Computing from the CNSI for the DFT calculation (NSF CNS-1725797). B.F.C. and G.N.M.R. gratefully acknowledge the financial support from Mitsubishi Chemical-Centre for Advanced Materials for the solid-state NMR analyses. Solid-state NMR experiments and advanced polymer chromatography were carried out at the Central Facilities and Shared Experimental Facilities, respectively, of the UCSB Materials Research Laboratory supported by the MRSEC program of the U.S. NSF under award no. DMR-1720256, which is a member of the NSF-funded Materials Research Facilities Network (www.mrfn.org). This research used beamline 7.3.3 of the Advanced Light Source, which is a DOE Office of Science User Facility under contract no. DE-AC02-05CH11231.

References:

1. Forrest, S. R. & Thompson, M. E. Introduction: Organic Electronics and Optoelectronics. *Chem. Rev.* **107**, 923–925 (2007).

2. Meier, H. Conjugated Oligomers with Terminal Donor–Acceptor Substitution. *Angew. Chem. Int. Ed.* **44**, 2482–2506 (2005).

3. Kim, F. S., Guo, X., Watson, M. D. & Jenekhe, S. A. High-mobility Ambipolar Transistors and High-gain Inverters from a Donor–Acceptor Copolymer Semiconductor. *Adv. Mater.* **22**, 478–482 (2010).

4. Dennler, G., Scharber, M. C. & Brabec, C. J. Polymer-Fullerene Bulk-Heterojunction Solar Cells. *Adv. Mater.* **21**, 1323–1338 (2009).

5. Uoyama, H., Goushi, K., Shizu, K., Nomura, H. & Adachi, C. Highly efficient organic light-emitting diodes from delayed fluorescence. *Nature* **492**, 234–238 (2012).

6. Kulkarni, A. P., Kong, X. & Jenekhe, S. A. High-Performance Organic Light-Emitting Diodes Based on Intramolecular Charge-Transfer Emission from Donor–Acceptor Molecules: Significance of Electron-Donor Strength and Molecular Geometry. *Adv. Funct. Mater.* **16**, 1057–1066 (2006).

7. Sun, Y. *et al.* Solution-processed small-molecule solar cells with 6.7% efficiency. *Nat. Mater.* **11**, 44–48 (2012).
8. Yau, C. P. *et al.* Influence of the Electron Deficient Co-Monomer on the Optoelectronic Properties and Photovoltaic Performance of Dithienogermole-based Co-Polymers. *Adv. Funct. Mater.* **24**, 678–687 (2014).
9. Wang, M. *et al.* Hole Mobility and Electron Injection Properties of D-A Conjugated Copolymers with Fluorinated Phenylene Acceptor Units. *Adv. Mater.* **29**, 1603830 (2017).
10. Welch, G. C., Coffin, R., Peet, J. & Bazan, G. C. Band Gap Control in Conjugated Oligomers via Lewis Acids. *J. Am. Chem. Soc.* **131**, 10802–10803 (2009).
11. Poverenov, E., Zamoshchik, N., Patra, A., Ridelman, Y. & Bendikov, M. Unusual Doping of Donor–Acceptor-Type Conjugated Polymers Using Lewis Acids. *J. Am. Chem. Soc.* **136**, 5138–5149 (2014).
12. Welch, G. C. & Bazan, G. C. Lewis Acid Adducts of Narrow Band Gap Conjugated Polymers. *J. Am. Chem. Soc.* **133**, 4632–4644 (2011).
13. Hansmann, M. M. *et al.* B(C6F5)3: A Lewis Acid that Brings the Light to the Solid State. *Angew. Chem. Int. Ed.* **55**, 1196–1199 (2016).
14. Yamaguchi, K., Murai, T., Guo, J.-D., Sasamori, T. & Tokitoh, N. Acid-Responsive Absorption and Emission of 5-N-Arylaminothiazoles: Emission of White Light from a Single Fluorescent Dye and a Lewis Acid. *ChemistryOpen* **5**, 434–438 (2016).
15. Randell, N. M., Fransishyn, K. M. & Kelly, T. L. Lewis Acid–Base Chemistry of 7-Azaisoindigo-Based Organic Semiconductors. *ACS Appl. Mater. Interfaces* **9**, 24788–24796 (2017).
16. Zalar, P., Henson, Z. B., Welch, G. C., Bazan, G. C. & Nguyen, T.-Q. Color Tuning in Polymer Light-Emitting Diodes with Lewis Acids. *Angew. Chem.* **124**, 7613–7616 (2012).
17. Lin, J. *et al.* Heteroatomic Conjugated Polymers and the Spectral Tuning of Electroluminescence via a Supramolecular Coordination Strategy. *Macromol. Rapid Commun.* **37**, 1807–1813 (2016).

18. Zalar, P. *et al.* Increased Mobility Induced by Addition of a Lewis Acid to a Lewis Basic Conjugated Polymer. *Adv. Mater.* **26**, 724–727 (2014).

19. Pingel, P. *et al.* p-Type Doping of Poly(3-hexylthiophene) with the Strong Lewis Acid Tris(pentafluorophenyl)borane. *Adv. Electron. Mater.* **2**, (2016).

20. Ye, T., Wang, J., Chen, W., Yang, Y. & He, D. Improved Performance and Reproducibility of Perovskite Solar Cells by Well-Soluble Tris(pentafluorophenyl)borane as a p-Type Dopant. *ACS Appl. Mater. Interfaces* **9**, 17923–17931 (2017).

21. Yan, H. *et al.* Lewis Acid Doping Induced Synergistic Effects on Electronic and Morphological Structure for Donor and Acceptor in Polymer Solar Cells. *Adv. Energy Mater.* **8**, 1703672 (2018).

22. Han, Y. *et al.* Doping of Large Ionization Potential Indenopyrazine Polymers via Lewis Acid Complexation with Tris(pentafluorophenyl)borane: A Simple Method for Improving the Performance of Organic Thin-Film Transistors. *Chem. Mater.* **28**, 8016–8024 (2016).

23. Panidi Julianna *et al.* Remarkable Enhancement of the Hole Mobility in Several Organic Small-Molecules, Polymers, and Small-Molecule:Polymer Blend Transistors by Simple Admixing of the Lewis Acid p-Dopant B(C6F5)3. *Adv. Sci.* **5**, 1700290 (2017).

24. Lee, J. *et al.* A Planar Cyclopentadithiophene–Benzothiadiazole-Based Copolymer with sp2-Hybridized Bis(alkylsulfanyl)methylene Substituents for Organic Thermoelectric Devices. *Macromolecules* **51**, 3360–3368 (2018).

25. Erker, G. Tris(pentafluorophenyl)borane: a special boron Lewis acid for special reactions. *Dalton Trans.* **0**, 1883–1890 (2005).

26. E. Piers, W. & Chivers, T. Pentafluorophenylboranes: from obscurity to applications. *Chem. Soc. Rev.* **26**, 345–354 (1997).

27. W. E. Piers. The Chemistry of Perfluoraryl Boranes. *Adv. Organomet. Chem.* **52**, 1–76 (2005).

28. Blackwell, J. M., Piers, W. E., Parvez, M. & McDonald, R. Solution and Solid-State Characteristics of Imine Adducts with Tris(pentafluorophenyl)borane. *Organometallics* **21**, 1400–1407 (2002).

29. Focante, F., Mercandelli, P., Sironi, A. & Resconi, L. Complexes of tris(pentafluorophenyl)boron with nitrogen-containing compounds: Synthesis, reactivity and metallocene activation. *Coord. Chem. Rev.* **250**, 170–188 (2006).

30. Guidotti, S. *et al.* Synthesis and Reactivity of (C6F5)3B−N-Heterocycle Complexes. 1. Generation of Highly Acidic sp3 Carbons in Pyrroles and Indoles. *J. Org. Chem.* **68**, 5445–5465 (2003).

31. Hansen, M. R., Graf, R. & Spiess, H. W. Interplay of Structure and Dynamics in Functional Macromolecular and Supramolecular Systems As Revealed by Magnetic Resonance Spectroscopy. *Chem. Rev.* **116**, 1272–1308 (2016).

32. Dudenko, D. *et al.* A Strategy for Revealing the Packing in Semicrystalline π-Conjugated Polymers: Crystal Structure of Bulk Poly-3-hexyl-thiophene (P3HT). *Angew. Chem. Int. Ed.* **51**, 11068–11072 (2012).

33. Percec, V. *et al.* Self-Assembly of Dendronized Perylene Bisimides into Complex Helical Columns. *J. Am. Chem. Soc.* **133**, 12197–12219 (2011).

34. Seifrid, M. T., Reddy, G. N. M., Zhou, C., Chmelka, B. F., & Bazan, G. C. Direct Observation of the Relationship between Molecular Topology and Bulk Morphology for a π-Conjugated Material. *J. Am. Chem. Soc.* **141**, 5078–5082 (2019).

35. Reddy, G. N. M., Marsh, A., Davis, J. T., Masiero, S. & Brown, S. P. Interplay of Noncovalent Interactions in Ribbon-like Guanosine Self-Assembly: An NMR Crystallography Study. *Cryst. Growth Des.* **15**, 5945–5954 (2015).

36. R. Chaudhari, S. *et al.* Donor–acceptor stacking arrangements in bulk and thin-film high-mobility conjugated polymers characterized using molecular modelling and MAS and surface-enhanced solid-state NMR spectroscopy. *Chem. Sci.* **8**, 3126–3136 (2017).

37. Miller, N. C. *et al.* Use of X-Ray Diffraction, Molecular Simulations, and Spectroscopy to Determine the Molecular Packing in a Polymer-Fullerene Bimolecular Crystal. *Adv. Mater.* **24**, 6071–6079 (2012).

38. McGehee, M. D. *et al.* Role of molecular conformation at the donor-acceptor interface in organic photovoltaics. *Abstr. Pap. Am. Chem. Soc.* **247**, (2014).

39. Etzold, F. *et al.* Sub-ns triplet state formation by non-geminate recombination in PSBTBT:PC70BM and PCPDTBT:PC60BM organic solar cells. *Energy Environ. Sci.* **8**, 1511–1522 (2015).

40. Beringhelli, T., Maggioni, D. & D'Alfonso, G. 1H and 19F NMR Investigation of the Reaction of B(C6F5)3 with Water in Toluene Solution. *Organometallics* **20**, 4927–4938 (2001).

41. Skoog, D., Holler, F. & Crouch, S. *Principles of Instrumental Analysis*. (Brooks/Cole, Cengage Learning, 2007).

42. Connors, K. *Binding Constants: The Measurement of Molecular Complex Stability*. (John Wiley & Sons, 1987).

43. Turro, N., Ramamurthy, V. & Scaiano, J. *Modern Molecular Photochemistry of Organic Molecules*. (University Science Books, 2010).

44. Mikhnenko, O. V. *et al.* Trap-Limited Exciton Diffusion in Organic Semiconductors. *Adv. Mater.* **26**, 1912–1917 (2014).

45. Hušák, M. *et al.* Determining the Crystal Structures of Peptide Analogs of Boronic Acid in the Absence of Single Crystals: Intricate Motifs of Ixazomib Citrate Revealed by XRPD Guided by ss-NMR. *Cryst. Growth Des.* **18**, 3616–3625 (2018).

46. Peters, G. M. *et al.* G4-Quartet·M+ Borate Hydrogels. *J. Am. Chem. Soc.* **137**, 5819–5827 (2015).

47. Nelson, J. *Nuclear Magnetic Resonance Spectroscopy*. (Pearson Education, Inc., 2003).

48. Lee, B. H., Bazan, G. C. & Heeger, A. J. Doping-Induced Carrier Density Modulation in Polymer Field-Effect Transistors. *Adv. Mater.* **28**, 57–62 (2016).

49. Garcia, A. *et al.* Improvement of Interfacial Contacts for New Small-Molecule Bulk-Heterojunction Organic Photovoltaics. *Adv. Mater.* **24**, 5368–5373 (2012).

50. Reddy, G. N. M. *et al.* Co-existence of Distinct Supramolecular Assemblies in Solution and in the Solid State. *Chem. – Eur. J.* **23**, 2315–2322 (2017).

51. Melnyk, A. *et al.* Macroscopic Structural Compositions of π-Conjugated Polymers: Combined Insights from Solid-State NMR and Molecular Dynamics Simulations. *J. Phys. Chem. Lett.* **8**, 4155–4160 (2017).

52. Lo, C. K. *et al.* Every Atom Counts: Elucidating the Fundamental Impact of Structural Change in Conjugated Polymers for Organic Photovoltaics. *Chem. Mater.* **30**, 2995–3009 (2018).

53. Cochran, J. E. *et al.* Molecular Interactions and Ordering in Electrically Doped Polymers: Blends of PBTTT and F4TCNQ. *Macromolecules* **47**, 6836–6846 (2014).

54. Reddy, G. N. M., Kumar, M. V. V., Row, T. N. G. & Suryaprakash, N. N–H···F hydrogen bonds in fluorinated benzanilides: NMR and DFT study. *Phys. Chem. Chem. Phys.* **12**, 13232–13237 (2010).

55. Brédas, J.-L., Cornil, J. & Heeger, A. J. The exciton binding energy in luminescent conjugated polymers. *Adv. Mater.* **8**, 447–452 (1996).

56. Knupfer, M. Exciton binding energies in organic semiconductors. *Appl. Phys. A* **77**, 623–626 (2003).

57. Ran, N. A. *et al.* Harvesting the Full Potential of Photons with Organic Solar Cells. *Adv. Mater.* **28**, 1482–1488 (2016).

58. Zhao, Y., Guo, Y. & Liu, Y. 25th Anniversary Article: Recent Advances in n-Type and Ambipolar Organic Field-Effect Transistors. *Adv. Mater.* **25**, 5372–5391 (2013).

59. Zaumseil, J. & Sirringhaus, H. Electron and Ambipolar Transport in Organic Field-Effect Transistors. *Chem. Rev.* **107**, 1296–1323 (2007).

60. Greenham, N. C., Moratti, S. C., Bradley, D. D. C., Friend, R. H. & Holmes, A. B. Efficient light-emitting diodes based on polymers with high electron affinities. *Nature* **365**, 628–630 (1993).

61. Brown, T. M. *et al.* Efficient electron injection in blue-emitting polymer light-emitting diodes with LiF/Ca/Al cathodes. *Appl. Phys. Lett.* **79**, 174–176 (2001).

62. Rand, B. P., Burk, D. P. & Forrest, S. R. Offset energies at organic semiconductor heterojunctions and their influence on the open-circuit voltage of thin-film solar cells. *Phys. Rev. B* **75**, 115327 (2007).

63. Ying, L. *et al.* Regioregular Pyridal[2,1,3]thiadiazole π-Conjugated Copolymers. *J. Am. Chem. Soc.* **133**, 18538–18541 (2011).

64. Lakowicz, J. R. *Principles of Fluorescence Spectroscopy*. (Springer, 2006).

65. Greenham, N. C. *et al.* Measurement of absolute photoluminescence quantum efficiencies in conjugated polymers. *Chem. Phys. Lett.* **241**, 89–96 (1995).

66. Khitrin, A. & Fung, B. M. Design of heteronuclear decoupling sequences for solids. *J. Chem. Phys.* **112**, 2392–2398 (2000).

67. M. J. Frisch *et al. Gaussian 09*. (Gaussian, Inc., 2016).

68. Becke, A. D. Density-functional thermochemistry. III. The role of exact exchange. *J. Chem. Phys.* **98**, 5648–5652 (1993).

69. Chai, J.-D. & Head-Gordon, M. Long-range corrected hybrid density functionals with damped atom–atom dispersion corrections. *Phys. Chem. Chem. Phys.* **10**, 6615–6620 (2008).

70. Kronik, L., Stein, T., Refaely-Abramson, S. & Baer, R. Excitation Gaps of Finite-Sized Systems from Optimally Tuned Range-Separated Hybrid Functionals. *J. Chem. Theory Comput.* **8**, 1515–1531 (2012).

For Table of Contents Only:

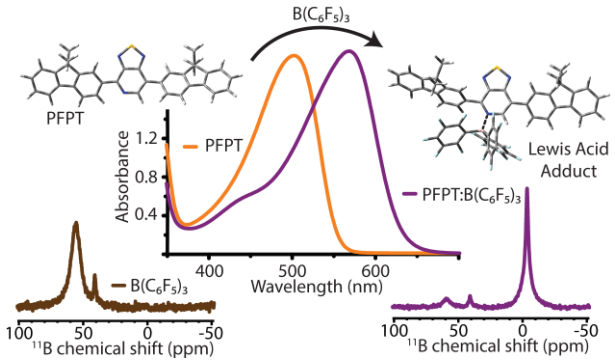

Atomic-Level Insight into the Post Synthesis Bandgap Engineering of a Lewis Basic Polymer Using the Lewis Acid Tris(pentafluorophenyl)borane

Brett Yurash,[§,†] Dirk Leifert,[§,†] G. N. Manjunatha Reddy,[‡] David Xi Cao,[†] Simon Biberger,[†,⊥] Viktor V. Brus,[†] Martin Seifrid,[†] Peter J. Santiago,[†] Anna Köhler,[⊥] Bradley F. Chmelka,[‡] Guillermo C. Bazan,*[,†] Thuc-Quyen Nguyen*[,†]

[†]Center for Polymers and Organic Solids, Department of Chemistry and Biochemistry
University of California, Santa Barbara, Santa Barbara, CA 93106, United States of America

[‡]Department of Chemical Engineering
University of California, Santa Barbara, Santa Barbara, CA 93106, United States of America

[⊥]Department of Physics, Bayreuth Institute of Macromolecular Research (BIMF) and Bavarian Polymer Institute (BPI), University of Bayreuth, Universitätsstraße 30, 95447 Bayreuth, Germany

[§]Co-first author

*Corresponding author's E-mail: quyen@chem.ucsb.edu, bazan@chem.ucsb.edu

Electronic Supplementary Information

Table of Contents

1. Electron paramagnetic resonance of PFPT:BCF

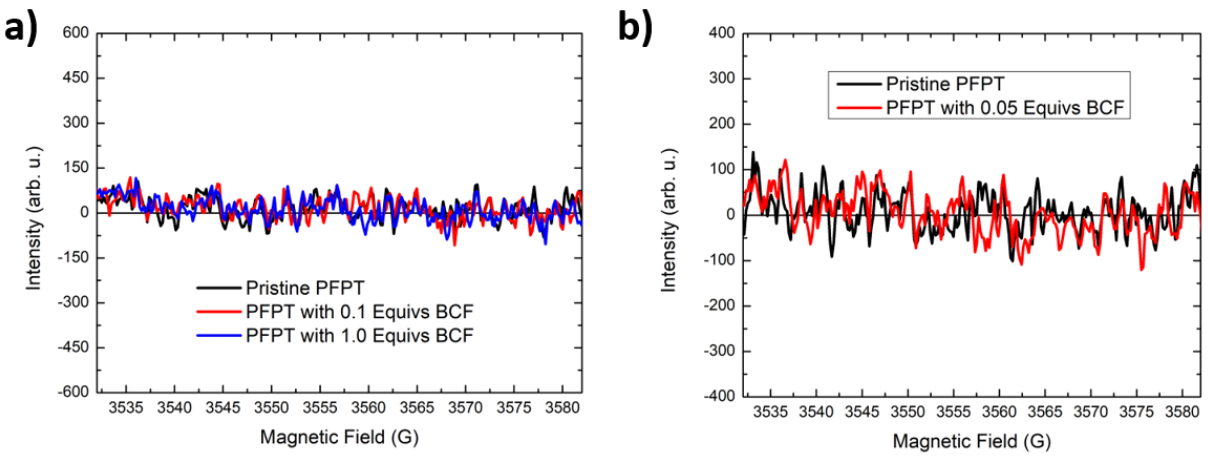

Figure S1. X-band EPR spectra of PFPT in solution (a) and solid state (b) with various amounts of BCF. Solutions for EPR were made at a polymer concentration of 0.125 mg/mL in chlorobenzene. No radicals were observed in solution or solid-state for PFPT. X-band Electron Paramagnetic Resonance measurements were performed on a Bruker EMX spectrometer with a ER041MR microwave bridge using a dielectric cavity. The sample was placed in a 0.8mm (inner diameter) round quartz capillary which was held in the cavity by a 4mm quartz EPR tube. The microwave power was 60mW, the modulation amplitude was 1 Gauss, and the modulation frequency was 100kHz. A concentrated solution was drawn into the capillary in the glovebox, both ends were sealed with Critoseal, and then brought out of the glovebox for measurements. Solid state samples were prepared in a similar manner, except that the solvent was allowed to evaporate from the capillary before sealing with Critoseal in the glovebox.

2. UV-Vis absorbance studies

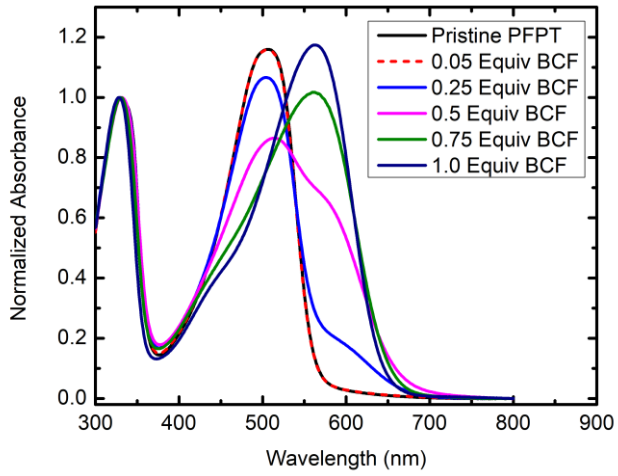

Figure S2. Absorption of thin films.

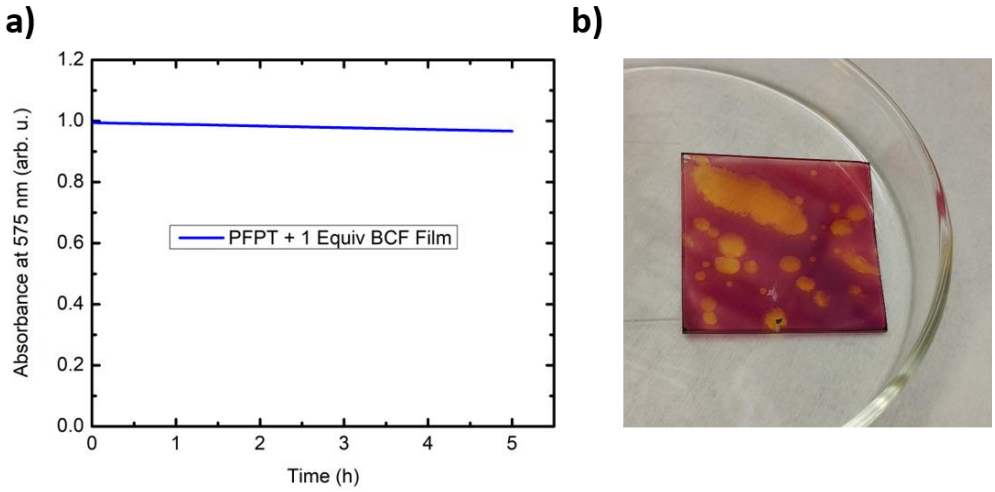

Figure S3. (a) Time-dependent absorption of a PFPT film with 1 equivalent of BCF exposed to air. After spin-coating in a nitrogen-filled glovebox, the sample was removed and the absorption measurement was immediately started. (b) Picture of film from (a) after 4 days left in the dark, but exposed to air. The orange spots correspond to pristine PFPT, whereas the dull purple areas correspond to the PFPT:BCF adduct.

3. DFT calculations of F-PT-F oligomer with and without BCF

Note on DFT calculations: Optimized structures calculated by density functional theory (DFT) using the B3LYP functional and 6-31G(d,p) basis set. Solvent effects were considered by using the SMD solvation model (solvent = chlorobenzene).

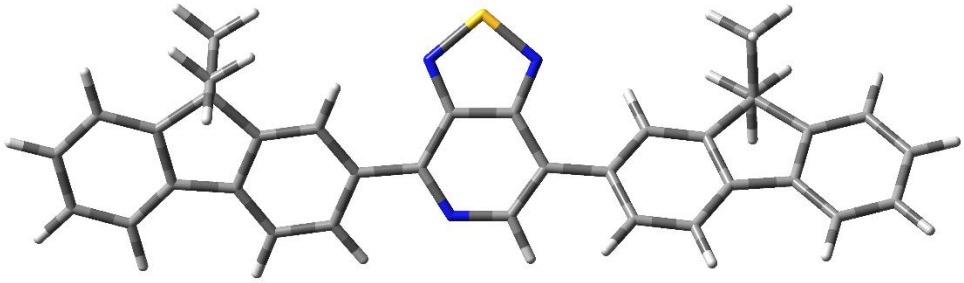

Figure S4. Optimized oligomer of PFPT. Dihedral angle of fluorene-PT on the right = -35°. Dihedral angle of fluorene-PT on the left (pyridyl side) = -18°.

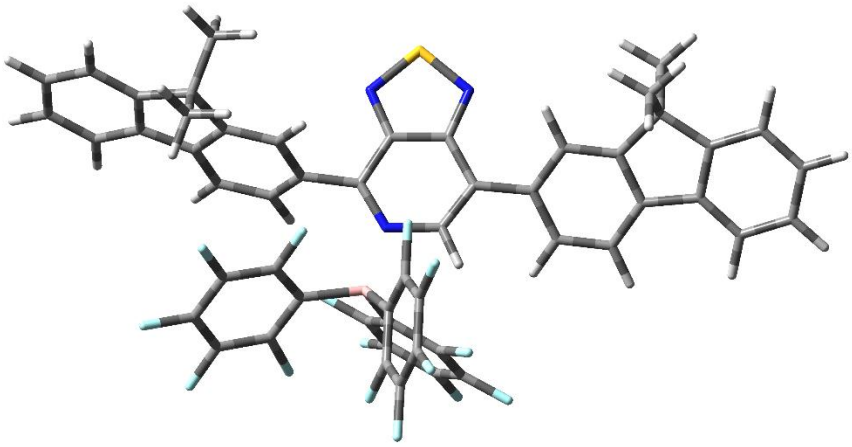

Figure S5. Optimized oligomer of PFPT with BCF coordinated to the pyridyl nitrogen. ΔU° = -0.08 eV. Dihedral angle of fluorene-PT on the right = 31°. Dihedral angle of fluorene-PT on the left (pyridyl side) = -74°. B-N distance is 1.69 Angstroms.

4. Photoluminescence studies

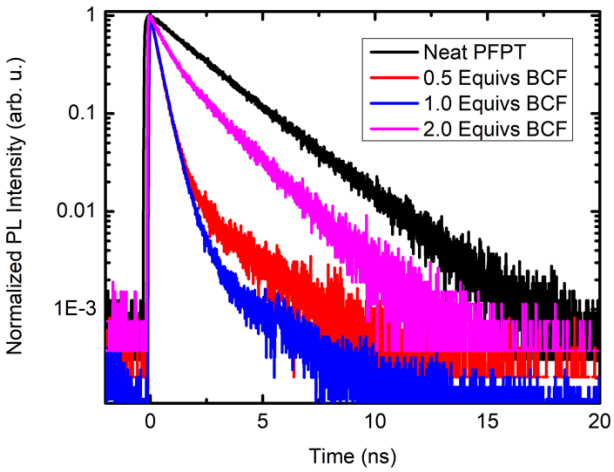

Figure S6. PL decays (710 nm detection wavelength) of PFPT in chlorobenzene with various amounts of BCF. An excitation wavelength of 400 nm was used.

The radiative (k_r) and nonradiative (k_{nr}) decay rates for pure PFPT in film and solution were calculated according to the following equation:

$$\Phi = \frac{k_r}{k_r + k_{nr}} = \tau \times k_r \qquad 1$$

where Φ is the measured PLQY and τ is the measured PL lifetime.

Table S1. Calculated rates of radiative and nonradiative decay for pure PFPT.

	Solution	Film
k_r (s^{-1})	3.3 x 10^8	2.2 x 10^8
k_{nr} (s^{-1})	1.1 x 10^8	1.8 x 10^9

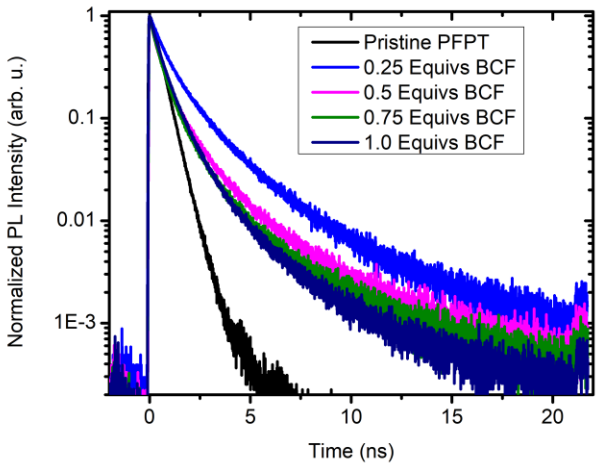

Figure S7. PL decays of PFPT:BCF films. An excitation wavelength of 400 nm was used. A detection wavelength of 705 nm was used for films with BCF. A detection wavelength of 580 nm was used for the pristine PFPT film.

5. Solution-state ^{11}B NMR of BCF:BT

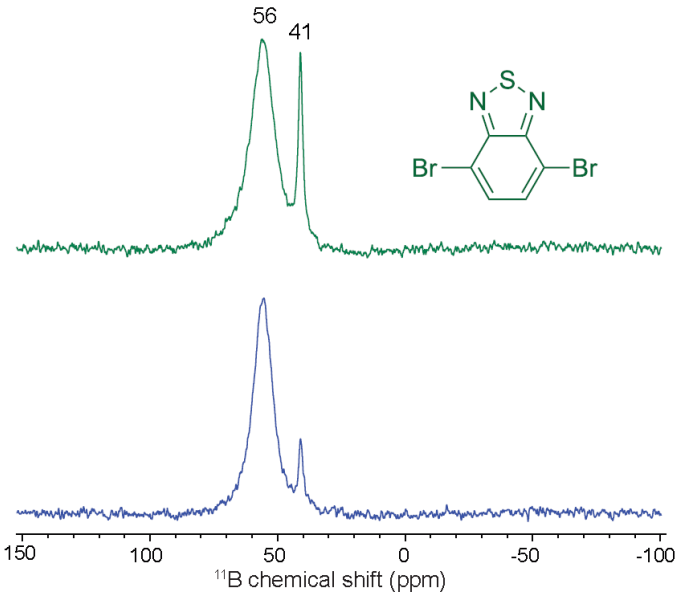

Figure S8. ^{11}B NMR spectra acquired at 11.7 T and at room temperature of 4,7-dibromobenzo[*c*]-1,2,5-thiadiazole (BT-Br_2) and 1 equivalent BCF in $CDCl_3$ (upper panel, green) and of neat BCF in $CDCl_3$ (lower panel, blue). The chemical structure of BT-Br_2 is also shown. Note the lack of any peaks near 0 ppm chemical shift, where a 4-coordinate boron atom is expected to exhibit resonance.

6. DFT calculations of BCF and F-PT-F:BCF complexes

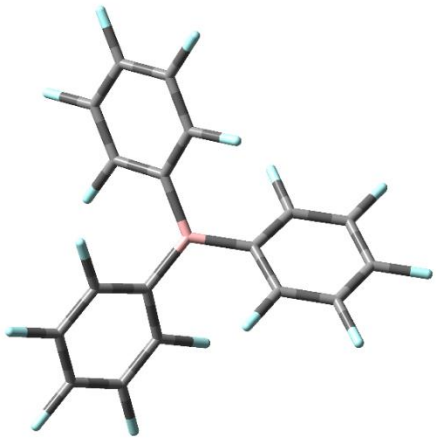

Figure S9. Optimized BCF structure with trigonal planar geometry of the boron atom.

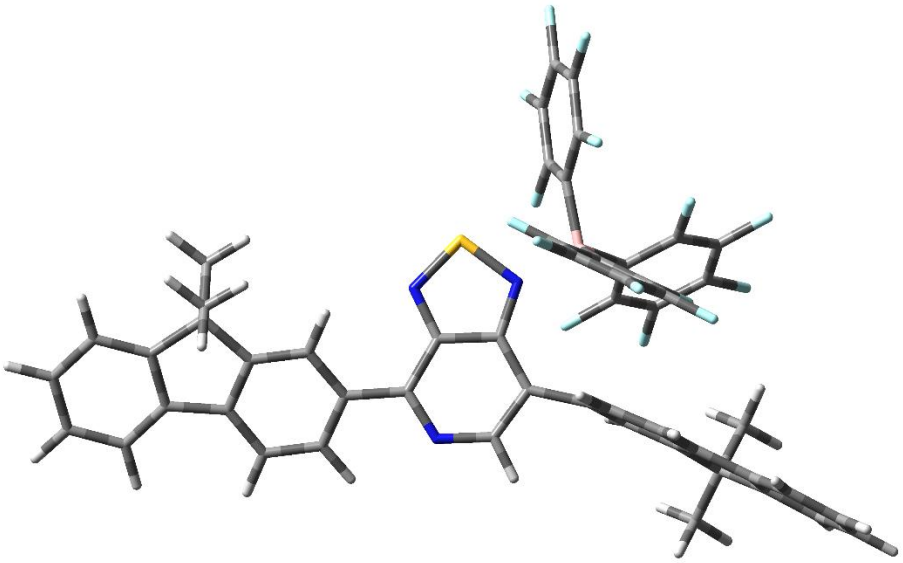

Figure S10. Optimized oligomer of PFPT with BCF coordinated to an azole nitrogen. $\Delta U° = 0.22$ eV. B-N distance is 1.67 Å.

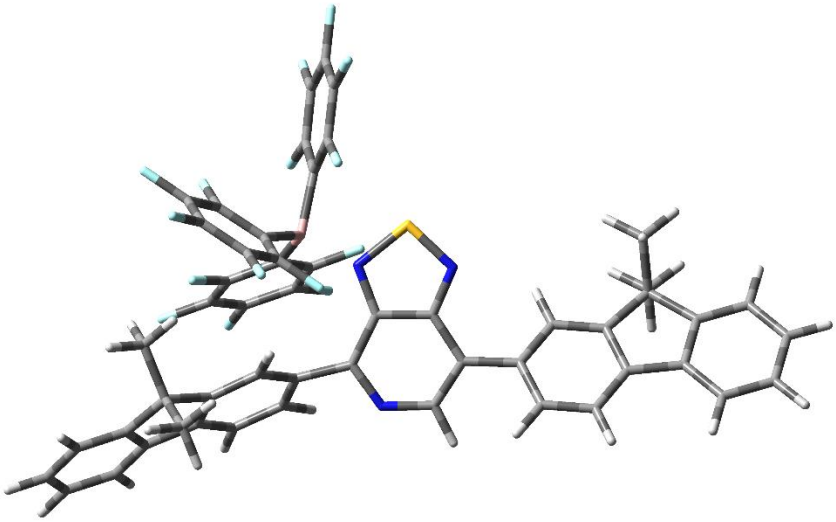

Figure S11. Optimized oligomer of PFPT with BCF coordinated to the other azole nitrogen. $\Delta U° = 0.47$ eV. B-N distance is 1.68 Å.

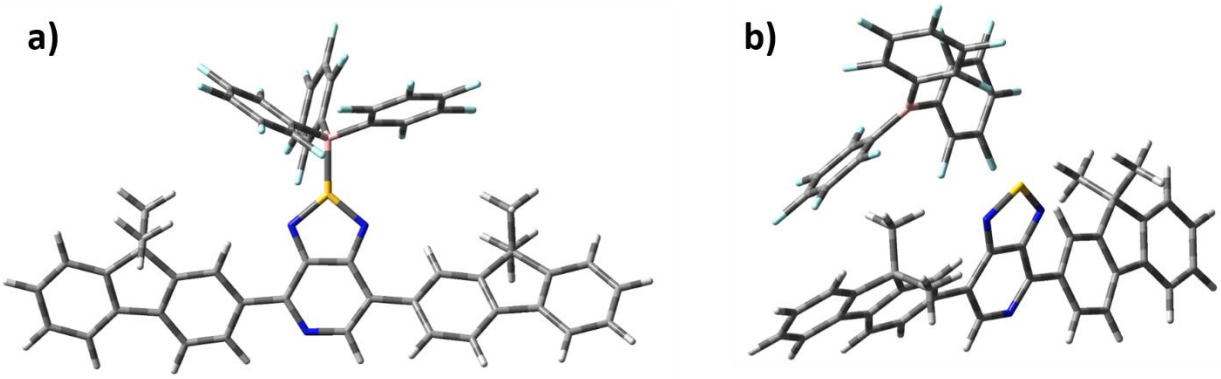

Figure S12. Attempted DFT geometry-optimization of PFPT with BCF coordinated to the sulfur atom. (a) Input geometry for DFT. (b) Optimized geometry of the converged structure that exhibits a B-S distance of 4.5 Å. The orientation of PFPT in (b) was chosen to more clearly show the distance of BCF relative to the oligomer and that BCF is in the trigonal planar geometry.

7. X-ray photoelectron spectroscopy measurements

X-ray photoelectron spectroscopy measurements of the pristine PFPT polymer and the polymer with 1 equivalent of BCF added support the results obtained from NMR spectroscopy. In Figure S15a, we see only the elements expected from the polymer in the survey scan of pristine PFPT. In addition, the survey scan is a confirmation that BCF is present in the film while the measurement is being obtained, as there is a strong fluorine signal from the BCF in the survey scan of pristine PFPT with one equivalent of BCF. In the high resolution C 1s XPS spectrum shown in Figure S15b, there is a peak located at 287.9 eV from the carbon bound to fluorine in BCF, which also confirms the presence of BCF in the film. In the C 1s XPS spectrum, the remainder of the envelope from 287 eV to 284 eV can be fit with three Voigt profiles, consistent with three inequivalent carbons in PFPT with the peak at 284.9 corresponding to aromatic C=C carbons, the peak at 285.1 corresponding to aliphatic C–C carbons, and the peak at 286.3 corresponding to the more electron poor carbon on the C–N bond, consistent with literature and the National Institutes of Science and Technology (NIST) XPS database.[1,2]

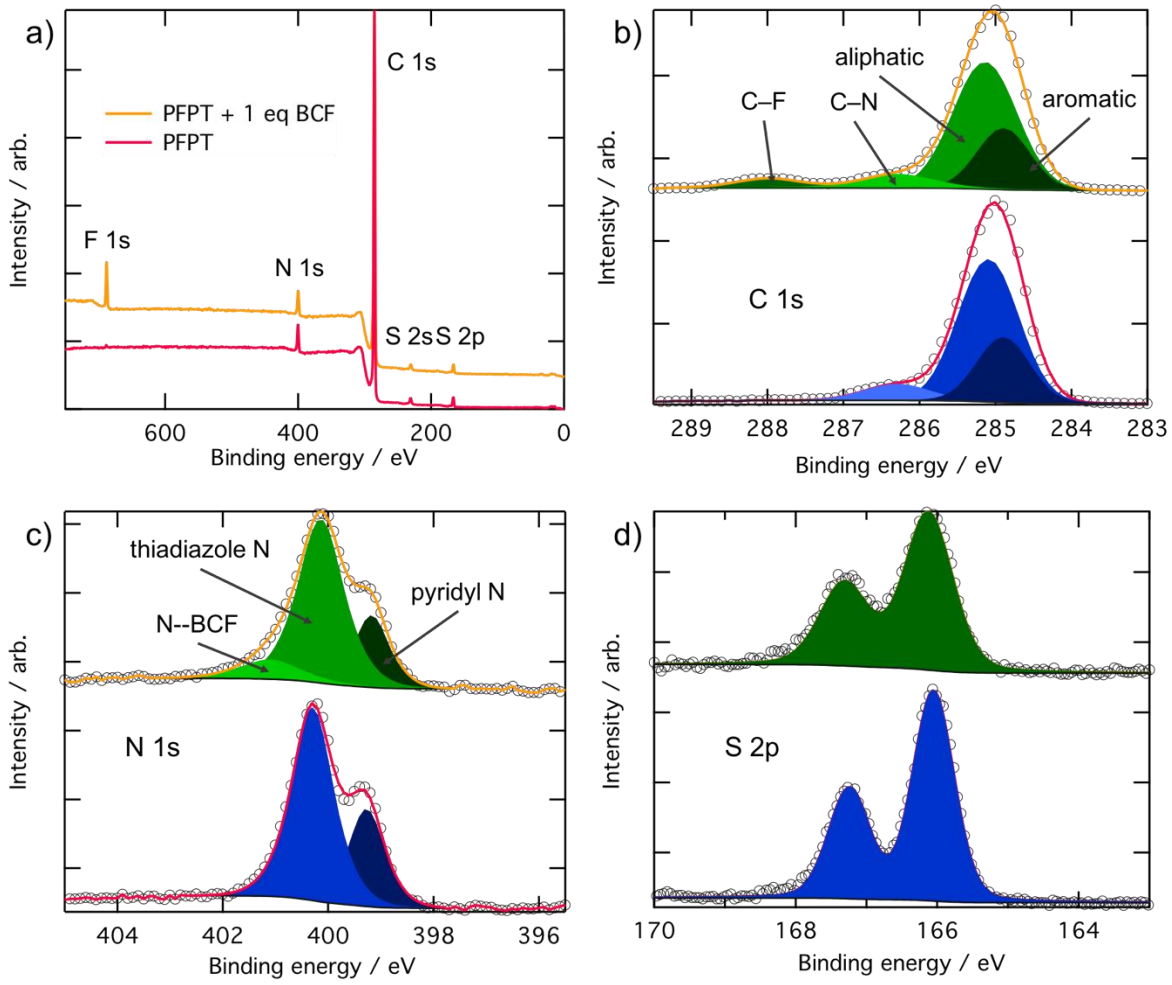

Figure S13. XPS spectra of PFPT and PFPT with 1 eq of BCF per PFPT monomer unit. Panel (a) shows the survey scan, and panels (b), (c), and (d) show the high-resolution XPS scans of C 1s, N 1s, and S 2p respectively.

The pristine PFPT nitrogen high-resolution XPS spectrum in Figure S15c shows two separate peaks from the Voigt fits of the main envelope. The peak at 399.2 eV corresponds to lone pyridyl nitrogen in PFPT, whereas the peak at 400.1 eV corresponds to the less electron rich thiadiazole nitrogens.[3,4] Upon addition of BCF to PFPT, we see the appearance of a new peak at 401.1 eV, which corresponds to a nitrogen bound to BCF. Because BCF is a Lewis acid, it withdraws electron density from the nitrogen atom, making it more electron poor and therefore causing the appearance of the new higher binding energy peak. The N–BCF peak also has a wider FWHM than the other nitrogen peaks, which is attributed to the additional N–BCF bond. The formation of the new N–BCF peak came at the expense of the pyridyl N peak, which strongly indicates BCF binding to the pyridyl N. While the peak percentage belonging to the thiadiazole N remained approximately the same within error, there was a reduction in the area of the pyridyl N peak (Table S2).

Table S2. Peak percentages from Voigt fits to N 1s high-resolution XPS spectra.

eV	0 eq. BCF	1 eq. BCF
399.2 eV	30 %	22 %
400.1 eV	70 %	68 %
401.1 eV	--	10.1 %

The pristine PFPT sulfur high-resolution XPS spectrum as well as the PFPT spectrum with 1 equivalent of BCF added both show only one S 2p doublet peak, corresponding to the thiadiazole sulfur (Figure S15d). This is a good indication that BCF does not bind to sulfur.

8. AFM, GIWAXS, and conductivity measurements

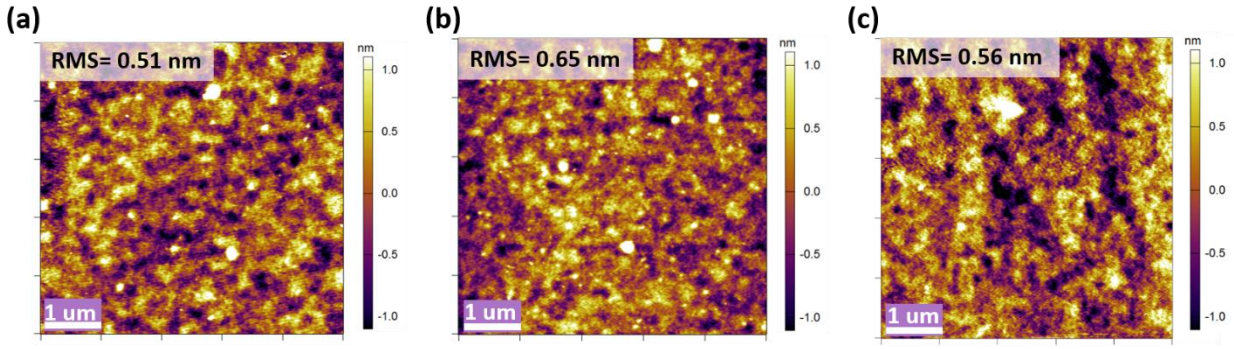

Figure S14. Atomic force microscope (AFM) images of (a) pristine PFPT, (b) PFPT with 0.05 molar equivalents BCF, and (c) 0.10 molar equivalents BCF. AFM images were obtained in tapping mode on an Asylum MFP-3D setup using a Pt/Cr coated silicon tip (Budget Sensors) with a resonance frequency of 75 kHz and a force constant of 3 N/m. All images were obtained using a 0.40 Hz scan rate at a 90 degree scan angle to account for tip geometry.

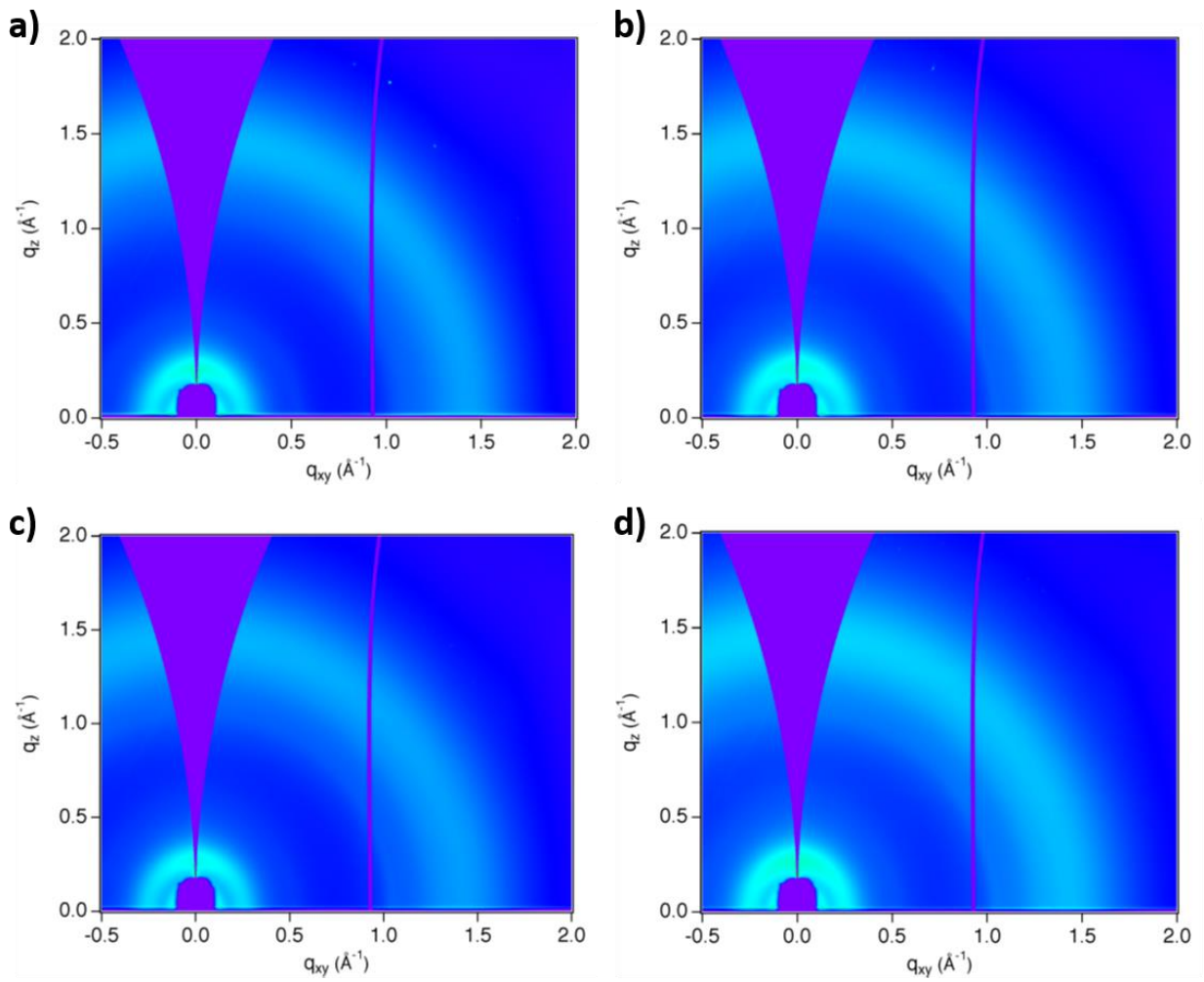

Figure S15. Grazing-incidence wide-angle X-ray scattering (GIWAXS) of PFPT with various amounts of BCF. (a) pristine PFPT, (b) 0.01 molar equivalents BCF, (c) 0.05 molar equivalents BCF, and (d) 0.10 molar equivalents BCF. Measurements were taken at beamline 7.3.3 of the Advanced Light Source with an X-ray wavelength of 1.2398 Å (10 keV) at a sample-detector distance of 274 mm. Measurements were calibrated using an Ag-behenate standard. Samples were scanned in a He environment at an incidence angle of 0.12°. Diffraction patterns were processed using the Nika software package for Wavemetrics Igor, in combination with a custom Igor script, WAXStools.

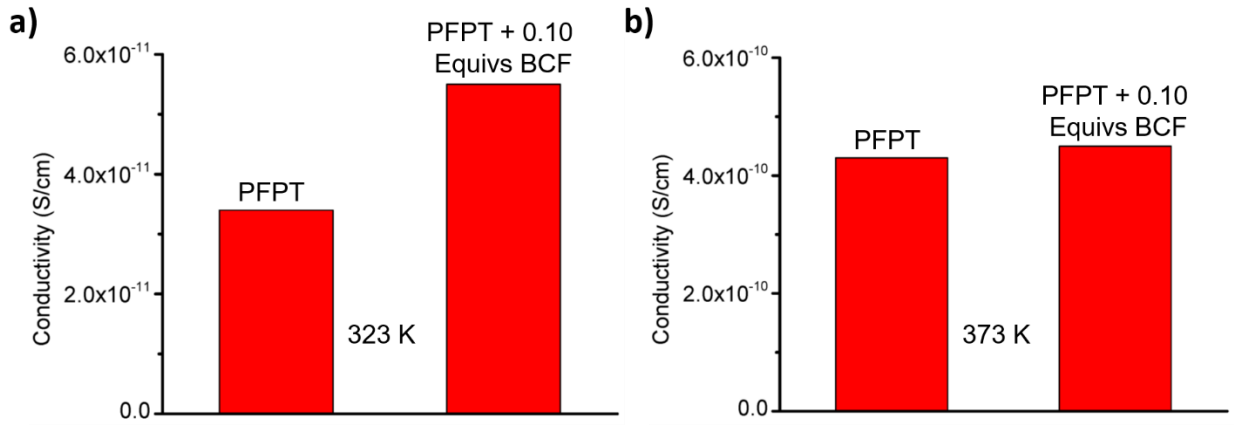

Figure S16. The conductivity of pristine PFPT and PFPT with 0.10 molar equivalents BCF was measured on substrates with interdigitated electrodes (electron beam evaporated platinum). Platinum was used as the electrode material due to its low work function (<6 eV). At room temperature, the conductivity of PFPT and PFPT with BCF was below the limit of detection. Thus, we measured conductivity at elevated temperatures, 323 K (a) and 373 K (b). Because the conductivity of PFPT is so low, it is difficult to assess the effect that BCF has on its electrical properties. The concentration of BCF is given as molar equivalents with respect to the repeat unit of the polymer.

9. Ultraviolet photoelectron spectroscopy (UPS) measurements

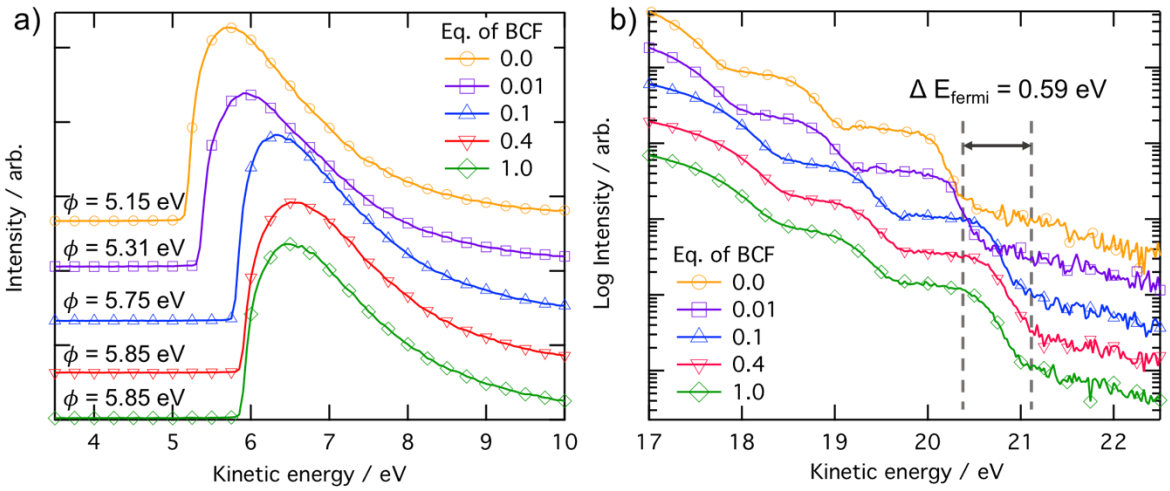

Figure S17. UPS spectra of (a) the photoemission onset, ϕ, and (b) the position of the leading edge of the HOMO for thin films of PFPT with different equivalents of BCF.

Table S3. Summary of results from UPS measurements on thin films.

Molar Equivalents of BCF	Work Function (eV)	Ionization Potential (eV)
0.00	-5.15	-6.05
0.01	-5.31	-6.06
0.10	-5.75	-6.05
0.40	-5.85	-6.10
1.00	-5.85	-6.15

10. Synthesis and characterization

4,7-Dibromo-[1,2,5]thiadiazolo[3,4-c]pyridine was purchased by Oxchem Corporation and Sunatech. A Biotage microwave reactor was used for polymerizations and endcapping.

Flash chromatography (FC) was carried out on Silicycle SiliaFlash P60 with an excess Argon pressure up to 0.5 bar. For thin layer chromatography (TLC) EMD Millipore Analytical Chromatography "TLC Silica gel 60 F254" with aluminum back were used with UV light (254/366 nm) for detection.

^{1}H-NMR (400 MHz and 500 MHz) and ^{13}C-NMR (101 MHz and 126 MHz) were measured on an actively-shielded Agilent Technologies 400-MR DDR2 400 MHz or a Varian Unity Inova 500 MHz spectrometer. The multiplicity of all signals was described by s (singlet), d (doublet), t (triplet) and m (multiplet).

Chemical shifts (δ in ppm) were referenced to the solvent residual peak of $CDCl_3$ (^{1}H-NMR: δ = 7.26; ^{13}C-NMR: δ = 77.0) or o-CD_4Cl_2 (^{1}H-NMR: δ = 6.812). HRMS ESI (m/z) measurements were performed on a Bruker Microflex LRF MALDI TOF mass spectrometer.

2,7-dibromo-9,9-dihexadecyl-9*H*-fluorene (S2)

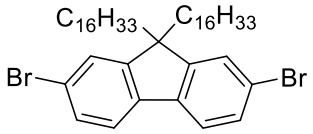

According to a literature procedure 2,7-dibromo-9*H*-fluorene (648.7 mg, 2.002 mmol, 1.0 eq.) and 1-bromohexadecane (1.3 mL, 4.3 mmol, 2.1 eq.) was dissolved in THF (4.0 mL, 0.5 M).[5] After fast addition (exothermic reaction) of KO*t*Bu (673.2 mg, 6.000 mmol, 3.0 eq.) the mixture was stirred for 40 h at 40 °C. Cold H_2O and brine was added to the mixture. The aqueous phase was extracted three times with diethylether. The combined organic phases were dried over $MgSO_4$, filtered and after removal of all sovents *in vacuo* the residue was subjected to FC (hexane). The white residue was melted in hot acetone and crystallized in the freezer twice. The desired alkylated fluorene **S2** (1.321 g, 1.709 mmol, 85%) was received as white solid.

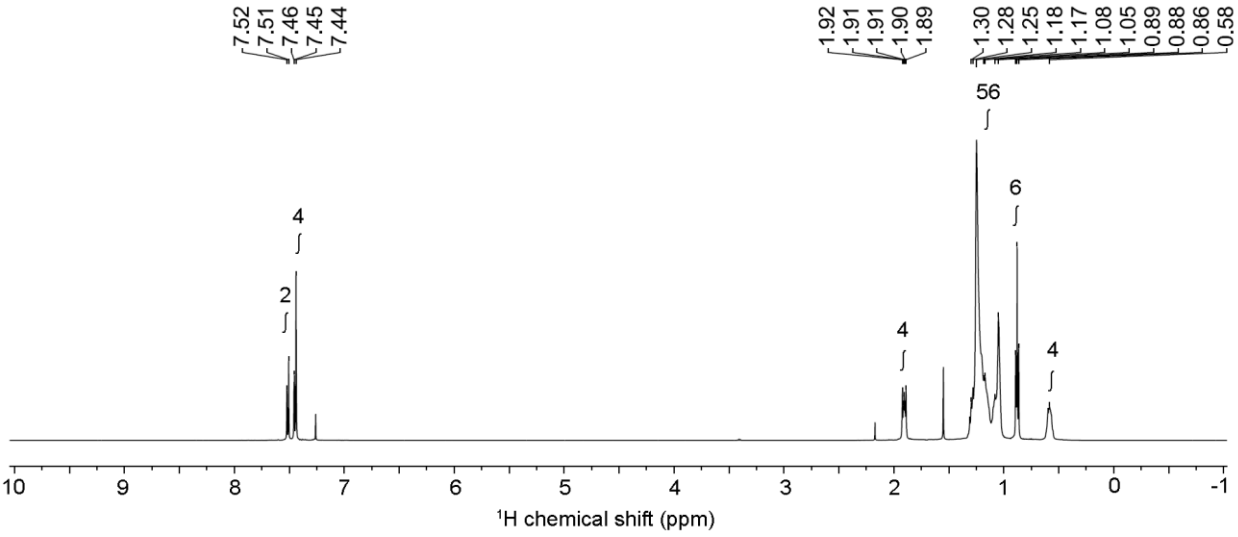

Figure S18. ^{1}H-NMR acquired at 11.7 T (500 MHz) and at 300 K of 2,7-dibromo-9,9-dihexadecyl-9*H*-fluorene in $CDCl_3$: δ (ppm) = 7.51 (d, *J* = 7.9 Hz, 2H), 7.47 – 7.43 (m, 4H), 1.93 – 1.88 (m, 4H), 1.32 – 1.01 (m, 56H), 0.88 (t, *J* = 6.9 Hz, 6H), 0.65 – 0.54 (m, *J* = 7.3 Hz, 4H). Spectroscopic data are in accordance with those described in the literature.[5]

(9,9-dihexadecyl-9*H*-fluorene-2,7-diyl)bis(trimethylstannane) (S3)

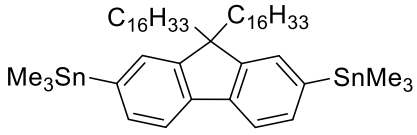

Dibromofluorene **S2** (846.8 mg, 1.096 mmol, 1.0 eq.) was dissolved in THF (5.5 mL, 0.20 M). At -78 °C a solution of *t*BuLi (1.7 M in pentane, 3.1 mL, 5.3 mmol, 4.8 eq.) was added over 10 minutes under vigorous stirring. Stirring was continued for 60 min. A solution of trimethyltinchloride (1.0 M in THF, 3.5 mL, 3.5 mmol, 3.2 eq.) was added and after 60 min at -78 °C the cooling bath was removed. After stirring overnight H_2O, brine and DEE was added. The organic phase was washed with $NaHCO_3$ (sat.), dried over $MgSO_4$ and filtrated. Removal of all volatiles *in vacuo* the distannane **S3** (977.2 mg, 1.039 mmol, 95%) was received as yellowish oil.

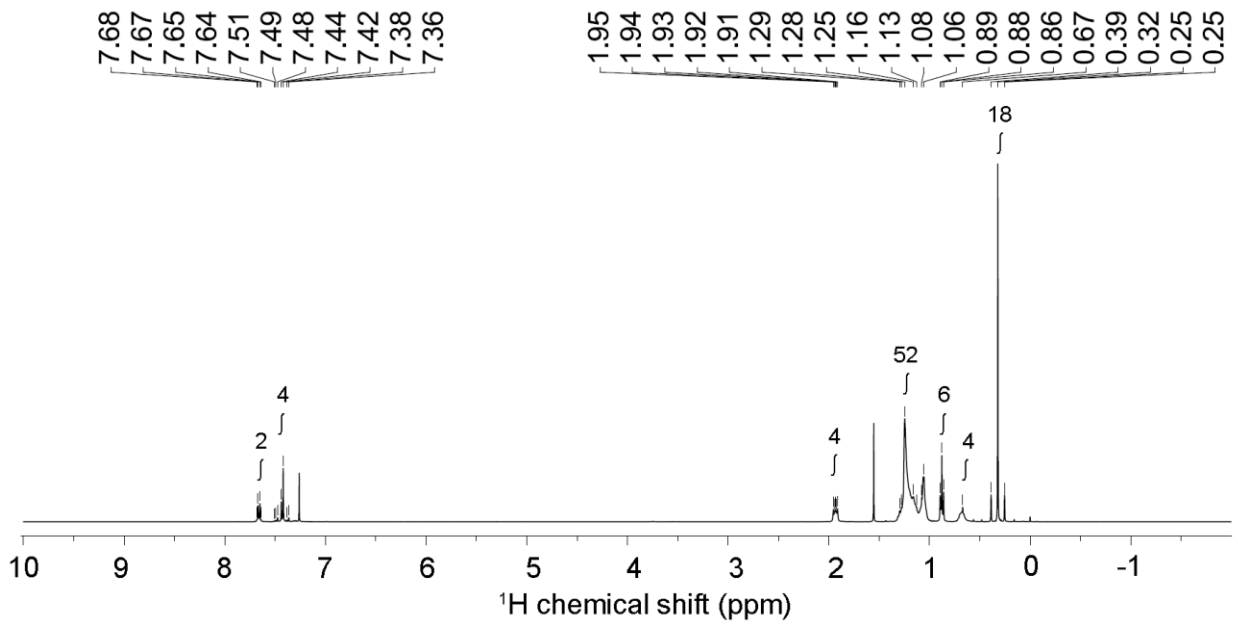

Figure S19. ^{1}H-NMR acquired at 9.4 T (400 MHz) and at 300 K of (9,9-dihexadecyl-9*H*-fluorene-2,7-diyl)bis(trimethylstannane) in $CDCl_3$: δ (ppm) = 7.69 – 7.63 (m, 2H, $C_{arom}H$), 7.51 – 7.35 (m, 4H, $C_{arom}H$), 1.98 – 1.89 (m, 4H, CH_2), 1.34 – 1.01 (m, 52H, CH_2), 0.88 (t, J = 6.8 Hz, 6H, CH_3), 0.75 – 0.61 (m, 4H, CH_2), 0.48 – 0.18 (m, 18H, CH_3).

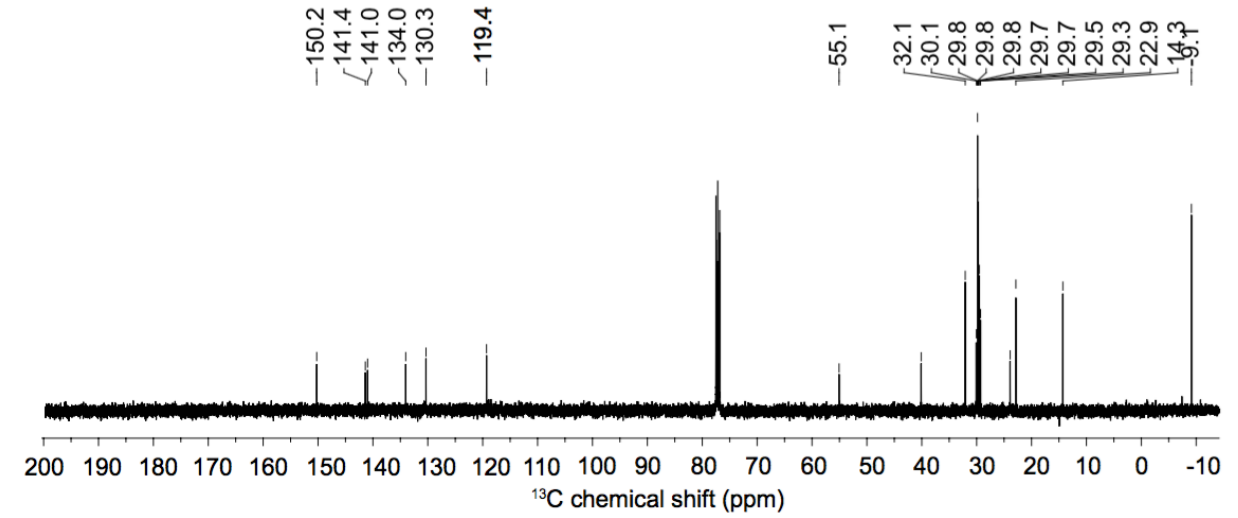

Figure S20. ^{13}C-NMR acquired at 11.7 T (126 MHz) and at 300 K of (9,9-dihexadecyl-9*H*-fluorene-2,7-diyl)bis(trimethylstannane) in $CDCl_3$: δ (ppm) = 150.2, 141.4, 141.0, 134.0, 130.3, 119.4, 55.1, 40.1, 32.1, 30.1, 29.8, 29.8, 29.8, 29.7, 29.7, 29.5, 29.3, 23.9, 22.9, 14.3, -9.1. HRMS (MALDI) *m/z* = 925.4 calcd. for $C_{50}H_{87}Sn_2^+$ $[M\text{-}CH_3]^+$, found: 925.5.

4,4'-(9,9-dihexadecyl-9*H*-fluorene-2,7-diyl)bis(7-bromo-[1,2,5]thiadiazolo[3,4-*c*]pyridine) (S4)

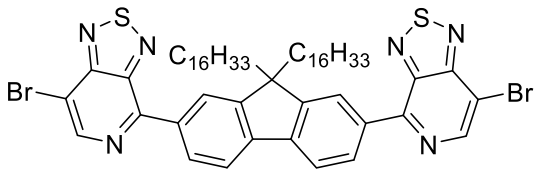

Fluorenedistannane **S3** (474.7 mg, 0.5046 mmol, 1.0 eq.), 4,7-Dibromo-[1,2,5]thiadiazolo[3,4-*c*]pyridine (339.6 mg, 1.151 mmol, 2.3 eq.) and $Pd(PPh_3)_4$ (72.3 mg, 69.3 µmol, 14 mol%) were dissolved in toluene (15 mL, 33 mM) and the reaction flask was sealed in the glove box. After stirring 22 h at 120 °C the mixture was filtered through a plug of silica/K_2CO_3 with chloroform/ethylacetate. The residue was purified by FC(Hex/CH_2Cl_2 = 2.5/1) and the desired product **S4** (178.3 mg, 0.1709 mmol, 34%) was received as orange solid.

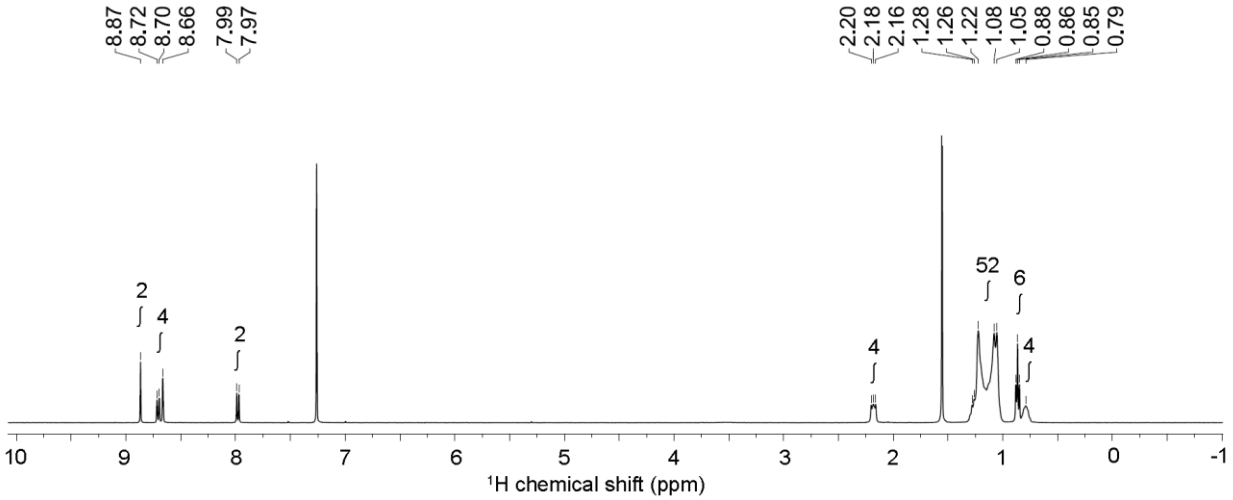

Figure S21. ^{1}H-NMR acquired at 9.4 T (400 MHz) and at 300 K of 4,4'-(9,9-dihexadecyl-9*H*-fluorene-2,7-diyl)bis(7-bromo-[1,2,5]thiadiazolo[3,4-*c*]pyridine) in $CDCl_3$: δ (ppm) = 8.87 (s, 2H, $C_{arom}H$), 8.71 (d, *J* = 8.0 Hz, 2H, $C_{arom}H$), 8.66 (s, 2H, $C_{arom}H$), 7.98 (d, *J* = 8.0 Hz, 2H, $C_{arom}H$), 2.25 – 2.14 (m, 4H, CH_2), 1.31 – 1.00 (m, 52H, CH_2), 0.86 (t, *J* = 6.8 Hz, 6H, CH_3), 0.83 – 0.74 (m, 4H, CH_3, CH_2).

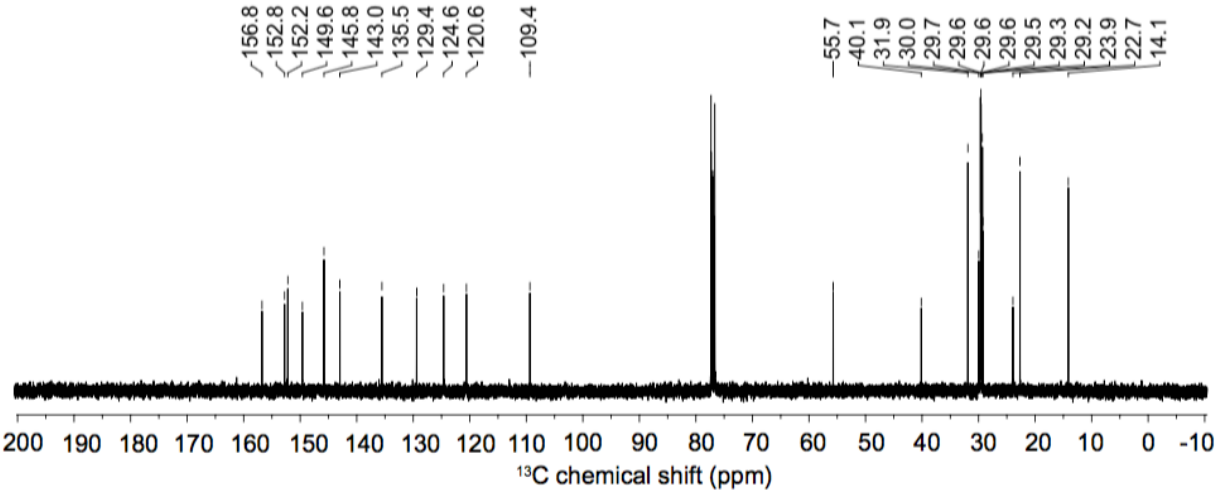

Figure S22. ^{13}C-NMR acquired at 9.4 T (101 MHz) and at 300 K of 4,4'-(9,9-dihexadecyl-9*H*-fluorene-2,7-diyl)bis(7-bromo-[1,2,5]thiadiazolo[3,4-*c*]pyridine) in $CDCl_3$: δ (ppm) = 156.8, 152.8, 152.2, 149.6, 145.8, 143.0, 135.5, 129.4, 124.6, 120.6, 109.4, 55.7, 40.1, 31.9, 30.0, 29.7, 29.6, 29.6, 29.6, 29.5, 29.3, 29.2, 23.9, 22.7, 14.1. HRMS (MALDI) *m/z*=1043.4 calculated for $C_{55}H_{75}Br_2N_6S_2^+$ $[M+H]^+$, found: 1043.3.

Poly[2,7-(9,9-bis(2-hexadecyl)-9*H*-fluorene)-*alt*-4,7-(9,9-dihexadecyl-9*H*-fluorene-2,7-diyl)bis[1,2,5]thiadiazolo[3,4-*c*]pyridine)] (PFPT)

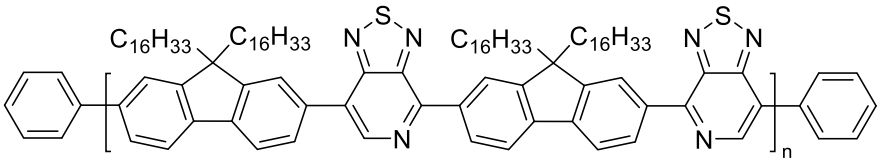

Dibromide **S4** (104.4 mg, 0.1105 mmol, 1.0 eq.), fluorenedistannane **S3** (99.0 mg, 0.105 mmol, 1.0 eq.) and $Pd(PPh_3)_4$ (6.0 mg, 5.2 µmol, 4.9 mol%) were dissolved in *o*-xylene/DMF (4.0 mL/0.40 mL, 24 mM) in a microwave tube and sealed in the glovebox. The reaction vessel was subjected to microwave reactor (80 °C 2 min, 120 °C 2 min, 160 °C 2 min, 180 °C 2 min, 200 °C 80 min; stirring: 900 rpm). For endcapping 2-tributylphenyltin (16 µL, 49 µmol, 0.47 eq.) and $Pd(PPh_3)_4$ (6.0 mg, 5.2 µmol, 4.9 mol%) were added and the flask was sealed in the glovebox. The microwave tube was subjected to microwave reactor (160 °C 50 min). Endcapping was repeated with bromobenzene (16 µL, 0.15 mmol, 1.4 eq.) and $Pd(PPh_3)_4$ (6.0 mg, 5.2 µmol, 4.9 mol%). The reaction mixture was precipitated in methanol and stirred overnight. After filtration the orange solid was subjected to a Soxhlet extraction using methanol, acetone, hexane and chloroform (collecting). After filtration through a paper filter the desired **PFPT** (115.3 mg, 73%) was received as orange solid. For upscaling this polymerization the amount of DMF was increased to ensure sufficient heating by the microwave reactor.

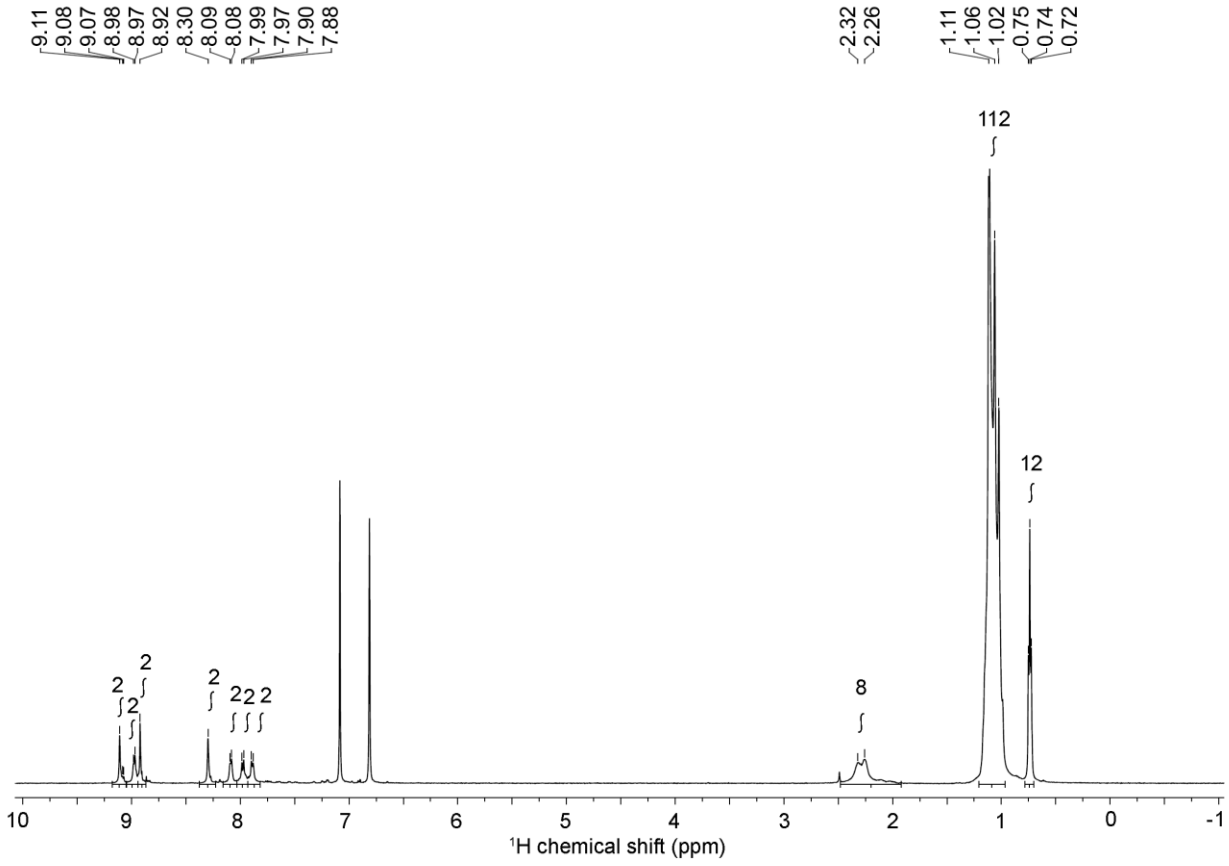

Figure S23. ^{1}H-NMR acquired at 11.7 T (500 MHz) and at 373 K of poly[2,7-(9,9-bis(2-hexadecyl)-9*H*-fluorene)-*alt*-4,7-(9,9-dihexadecyl-9*H*-fluorene-2,7-diyl)bis[1,2,5]thiadiazolo[3,4-*c*]pyridine)] in *o*-

CD_4Cl_2: δ (ppm) = 9.15 – 9.06 (m, 2H, $C_{arom}H$), 9.03 – 8.95 (m, 2H, $C_{arom}H$), 8.94 – 8.88 (m, 2H, $C_{arom}H$), 8.35 – 8.26 (m, 2H, $C_{arom}H$), 8.13 – 8.05 (m, 2H, $C_{arom}H$), 8.00 – 7.94 (m, 2H, $C_{arom}H$), 7.92 – 7.87 (m, 2H, $C_{arom}H$), 2.40 – 2.01 (m, 8H, CH_2), 1.18 – 0.96 (m, 112H, CH_2), 0.74 (t, J = 6.5 Hz, 12H, CH_3).

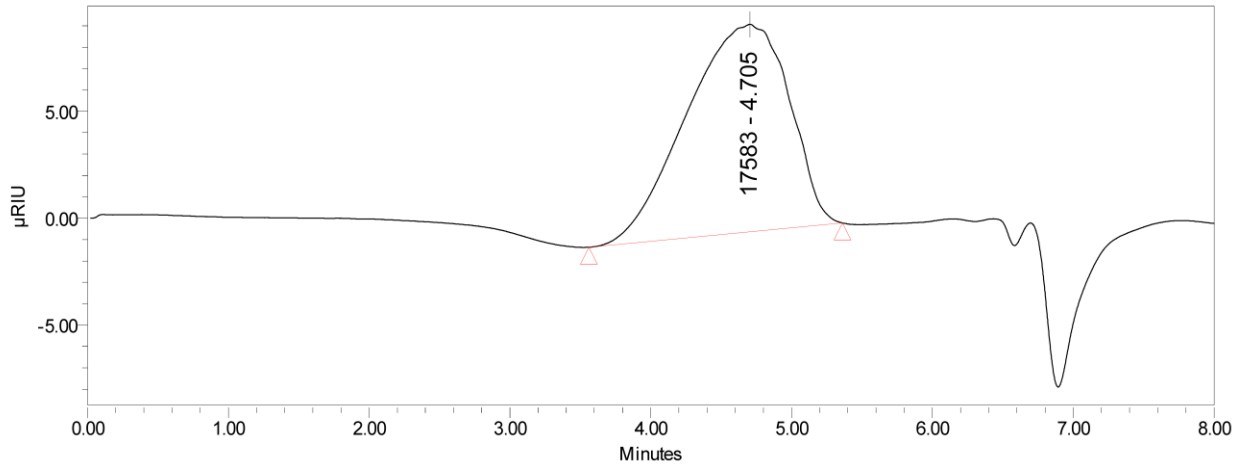

Figure S24. Advanced Polymer Chromatography of PFPT.

Advanced Polymer Chromatography (APC) was measured on a Waters® system consisting of a Waters Acquity APC pump, Acquity APC XT Columns (45 + 200 + 450 pore sizes) and a ACQUITY UPLC Refractive Index Detector. As solvent, chloroform containing 0.25% tetraethylamine was used with a flow rate of 0.5 mL/min, an injection volume of 25 µL and calibration versus a polystyrene standard.

Table S4. Results obtained from APC of PFPT.

M_n (g/mol)	M_w (g/mol)	M_p (g/mol)	M_z (g/mol)	M_z + 1 (g/mol)	Polydispersity
18461	25955	17583	36046	46823	1.41

11. References

1. Aygül, U. *et al.* Electronic Properties of Interfaces between PCPDTBT and Prototypical Electrodes Studied by Photoemission Spectroscopy. *ChemPhysChem* **12**, 2345–2351 (2011).
2. NIST X-ray Photoelectron Spectroscopy Database, Version 4.1. (2012).
3. Lee, B. H., Bazan, G. C. & Heeger, A. J. Doping-Induced Carrier Density Modulation in Polymer Field-Effect Transistors. *Adv. Mater.* **28**, 57–62 (2016).
4. Garcia, A. *et al.* Improvement of Interfacial Contacts for New Small-Molecule Bulk-Heterojunction Organic Photovoltaics. *Adv. Mater.* **24**, 5368–5373 (2012).
5. Liu, X.-G. & Sun, W. Platinum(II) Complexes Bearing 2-(9,9-Dihexadecyl-7-R-fluoren-2-yl)-1,10-phenanthroline Ligands: Synthesis, Photophysics and Reverse Saturable Absorption. *Eur. J. Inorg. Chem.* **2013**, 4732–4742 (2013).